International Journal of Solids and Structures 49 (2012) 973–988

Contents lists available at SciVerse ScienceDirect

International Journal of Solids and Structures

journal homepage: www.elsevier.com/locate/ijsolstr

Steady-state dynamics of a 3D tensegrity structure: Simulations and experiments

J. Michielsen *, R.H.B. Fey, H. Nijmeijer

Department of Mechanical Engineering, Eindhoven University of Technology, P.O. Box 513, 5600 MB Eindhoven, The Netherlands

ARTICLE INFO

Article history:
Received 27 July 2011
Received in revised form 7 November 2011
Available online 11 January 2012

Keywords:
Tensegrity structure
Steady-state analysis
Stability
Buckling
Piecewise linear
Path-following
Bifurcations
Experiments

ABSTRACT

This paper considers a modeling and analysis approach for the investigation of the linear and nonlinear steady-state dynamics of a base excited 3D tensegrity module carrying a top mass. The tensegrity module contains three compressive members, which may buckle and six cables (tendons). First, a dynamic model of the system is derived using Lagrange's equation with constraints. The buckling modeling of the compressive members is based on the assumed-mode method with a single mode discretization. The tendons are modeled as piecewise linear springs, which can only take tensile forces. This research focusses on the dynamic stability of the tensegrity structure by defining the geometrical and material properties in such a way that the system is just below the static stability boundary. Static and linear dynamic analysis is performed. In the nonlinear steady-state analysis, frequency-amplitude plots, power spectral density plots, bifurcation point continuation diagrams, and Poincaré maps are presented. A tensegrity structure is designed and manufactured and an experimental set-up is realized in order to validate the model by comparing experimentally and numerically obtained responses. In the validation stage, the numerical results are based on an amplifier-shaker-tensegrity structure model. It can be concluded that the numerical results match partly quantitatively and partly qualitatively with the experimentally obtained responses.

1. Introduction

Tensegrity structures originate from sculptures designed by Snelson (1973). This class of structures consists of a set of pin-jointed bodies (compressive members) and cables (tensile members), also called tendons, which ensure structural integrity by defining a stable volume in space. Inspired by these sculptures, Buckminster Fuller first patented these types of structures by combining the words *tension* and *integrity* to tensegrity in 1962 (Fuller, 1962). A historical survey of tensegrity structures is provided by Motro (1992).

Due to a favorable high stiffness/mass ratio, tensegrity structures have been introduced as potential alternatives in civil, aerospace, and mechanical engineering. Suspension bridges are classical examples of tensegrity based structures because the tensile components are often cables. More recently, designs similar to the sculptures of Kenneth Snelson are found in bridge designs. The Kurilpa bridge in Brisbane, Australia, is a perfect example. In addition, new applications in civil engineering are tensegrity grid structures used in roof designs, see Adriaenssens and Barnes (2001) and Quirant et al. (2003). Hypar tensegrity roofs can, for example, be found in sports stadiums in Florida, Georgia, and Seoul. Tensegrity structures are also used in fast robotic applications because of their low mass, see e.g. Aldrich (2004) and Masic and Skelton (2004). But the advantage of tensegrity structures goes beyond mass efficiency. The usage of tendons provides the possibility to fold a tensegrity structure in a small volume of space for transportation purposes. This key feature is of particular interest in aerospace applications (Furuya, 1992). A review of self-deploying tensegrity structures is presented in Duffy et al. (2000). Moving tensegrity mechanisms can be found in several applications, such as a flight simulator (Sultan and Corless, 2000), a space telescope (Sultan et al., 1999), and a smart sensor (Sultan and Skelton, 2004). Controlled tensegrity systems provide the possibility to make buildings responsive to earthquakes, severe winds, and thermal loads. The control of a tensegrity structure with three compressive members and nine tendons is studied in Kanchanasaratool and Williamson (2002).

Despite these advantages, tensegrity structures, just like other structures, may become unstable due to additional dynamic loads. In the worst case, this may result in failure of the system. The influence of dynamic loads on tensegrity structures can be investigated by developing sufficiently accurate mathematical models and analysis strategies. In general, in order to apply tensegrity structures in structural designs, it is vital to be able to predict, understand, and eventually optimize the static and dynamic stability of such systems. Design criteria in structural design often involve a low mass,

* Corresponding author. Tel.: +31 623508134.
E-mail address: j.michielsen@tue.nl (J. Michielsen).

0020-7683/$ - see front matter © 2012 Elsevier Ltd. All rights reserved.
doi:10.1016/j.ijsolstr.2011.12.011

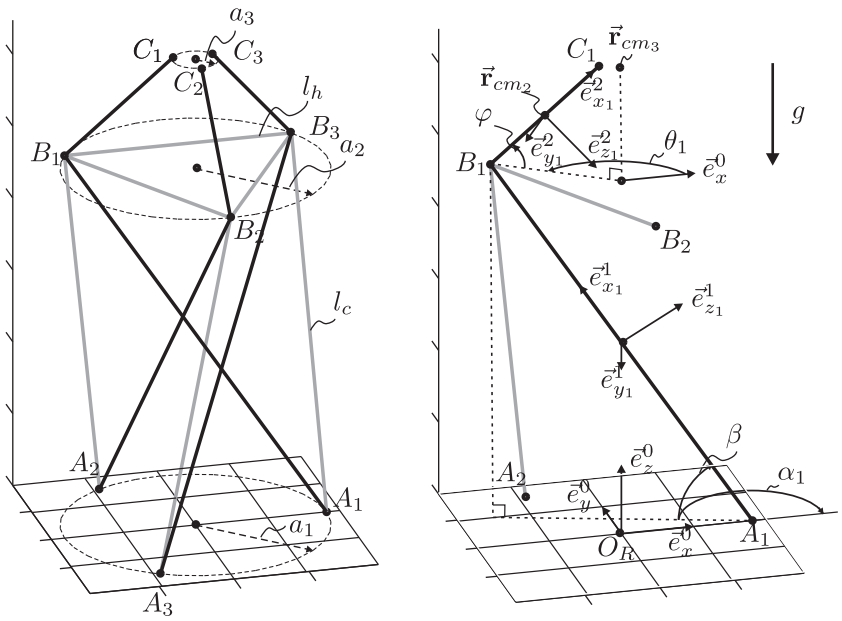

Fig. 1. The definition of the geometry, beams, struts, tendons, and nodes of the tensegrity structure (upper figure) and the reference frames (lower figure). In both figures, the top mass is not depicted.

a high stiffness, and a high residual strength. For tensegrity structures, these design criteria are mainly influenced by two important design parameters, namely the thickness of the compressive members and the amount of pretension in the tendons. When resonances occur, the compressive members of the tensegrity structure may dynamically buckle, although the system is statically stable. Static and dynamic buckling can be avoided by adopting a relatively high bending stiffness of the compressive members but this may also lead to an increase of the mass of the tensegrity structure. A high pretension in the tendons, in general, leads to high stiffness and avoidance of slackening of the tendons when resonances occur. But it also leads to lower residual strength and decreased static and dynamic stability of the structure because the allowed additional load of the compressive members decreases. This all leads to trade-offs in design choices. One can conclude that, constructing a tensegrity structure just below the static stability boundary, in order to avoid superfluous use of material, only makes sense if there is enough safety margin to avoid dynamic buckling of compressive members and slackening of tendons, which may be caused by additional dynamic loads. Nonlinear dynamic analysis of tensegrity structures can be used to predict dynamic buckling due to nonlinear resonances. Additionally, in the event of dynamic buckling of one or more compressive members, it can be used to evaluate if the structure does or does not globally collapse.

The Lagrangian approach has been frequently used for dynamic modeling of tensegrity structures. A linear dynamical model of a tensegrity structure with three compressive members and six tendons is studied to investigate the energy dissipation efficiency by solving initial value problems in Oppenheim and Williams (2001). The dynamics of a tensegrity structure with three compressive members and a six-module tensegrity structure are examined using the eigenmodes of the linearized dynamical model in Murakami (2001a). In addition, the nonlinear equilibrium equations are used to estimate the critical loads for static compressive member buckling and slackening of tendons in Murakami (2001b). The static stability due to external loads/moments of a tensegrity structure with three compressive members and six tendons is studied in Lazopoulos (2005) by evaluating the global instability of the model and local Euler buckling of the compressive members. Skelton (2006) suggested to describe the dynamics in a matrix differential equation instead of a vector differential equation. When using this method, the forces are characterized by network theory and the kinematics are expressed in terms of the compressive member vectors. This approach can only be applied to *Class 1* tensegrity structures, i.e. the compressive members are not allowed to be in contact with each other.

This paper deals with the static and dynamic stability of a tensegrity structure with three compressive members and six tendons carrying a top mass (and a top mass supporting structure). The compressive members of the tensegrity module are allowed to buckle statically and dynamically in a predefined direction. A dynamical model of the tensegrity structure is derived using Lagrange's equation of motion with constraints. The resulting equations of motion are used to study the static and (nonlinear) dynamic responses by loading the system with a top mass and, in the dynamic case, by additional periodic base excitation. In the second part of this paper, the model, which is first extended by an amplifier-shaker model, is validated by comparing numerically and experimentally obtained responses. From this analysis, it can be concluded that the modeling approach results in a model that matches partly quantitatively and partly qualitatively with the dynamical behavior of the experimental set-up. Consequently, the model can be used as a starting point to examine the origin of nonlinear dynamic response phenomena of tensegrity structures in general.

This paper is organized as follows. The geometric description of the tensegrity structure is discussed in Section 2. Buckling modeling of the compressive members of the tensegrity module is presented in Section 3. The equations of motion of the tensegrity structure are derived in Section 4. The geometrical and material properties are defined in Section 5. In Section 6, static response results are presented and analyzed to determine a suitable top mass. Modal analysis results and Frequency Response Functions (FRFs) are presented in Section 7 and in Section 8, respectively. This is followed by a detailed numerical study of nonlinear dynamic steady-state responses, initialized by periodic base excitation, in Section 9. The results from Sections 6–9 lay the foundations for the design of an experimental set-up. In Section 10, the experimental set-up is introduced and the corresponding amplifier-shaker-tensegrity model is defined. In Section 11, parameter identification is carried out. The model of the tensegrity structure is validated by comparing experimentally and numerically obtained linear and nonlinear dynamic responses in Section 12. Finally, the conclusions of this paper are presented in Section 13.

2. Description of the geometry

Fig. 1 shows the geometry and the reference frames of the tensegrity structure under consideration. Here, compressive members are indicated by black lines and tendons by gray lines. A Cartesian reference frame $\vec{\mathbf{e}}^0 = [\vec{e}_x^0 \;\; \vec{e}_y^0 \;\; \vec{e}_z^0]^T$ is connected to the absolute origin O_A with position vector $\vec{r}_{O_A} = [0 \;\; 0 \;\; 0]\vec{\mathbf{e}}^0$. The position vector of the relative origin O_R, which is connected to the centre of the vertically moving base of the structure containing nodes A_i for $i = 1,2,3$, is given by $\vec{r}_{O_R} = \vec{r}_{O_R} - \vec{r}_{O_A} = [0 \;\; 0 \;\; u(t)]\vec{\mathbf{e}}^0$, where $u(t)$ is the (periodic) vertical motion of the base.

Three compressive members are located between nodes A_i and B_i for $i = 1,2,3$. These compressive members will be called beams in the remainder of the paper because they are allowed to buckle. The uniform, homogeneous, pinned–pinned beams A_iB_i with rectangular cross section have length L_1, height H, width W, Young's modulus E, and mass density ρ_1. The buckling direction of beams A_iB_i is predefined in the $\vec{e}_{z_i}^1$ direction. Three other compressive members are located between nodes B_i and C_i for $i = 1,2,3$. These rigid compressive members are called struts. The uniform, homogeneous struts B_iC_i are cylindrically shaped with length L_2, radius R, and mass density ρ_2. A top mass (not visible in Fig. 1), modeled by a point mass m_3, is located at the centre of an imaginary circle through points C_1, C_2, and C_3. It is assumed that the top mass m_3 can only translate in vertical direction due to the design of the experimental set-up. Due to gravity g, the system is statically loaded in vertical direction by the weights of beams A_iB_i, struts B_iC_i, and by the weight of top mass m_3. As a result of the model assumptions, the system has a form of symmetry, because revolving the structure over 120° around the $\vec{e}_z^0$-axis results in an identical structure. Consequently, only one third of the structure needs to be modeled.

The absolute position vector of node A_i depends on radius a_1 and the position of the base $u(t)$

$$\vec{r}_{A_i} = [\, a_1 \cos\alpha_{0i} \quad a_1 \sin\alpha_{0i} \quad u(t)\,]^T \vec{\mathbf{e}}^0 \tag{1}$$

where $\alpha_{0i} = \frac{2\pi}{3}(i-1)$ for $i = 1,2,3$ defines the angle of node A_i in the horizontal plane. For each beam A_iB_i, two rotations $\alpha_i(t) = \alpha_{0i} + \alpha(t)$ (defined in the horizontal plane through nodes A_i) and $\beta(t)$ (defined in the plane through nodes A_i and B_i perpendicular to the horizontal plane), are used to express the reference frame $\vec{\mathbf{e}}_i^1 = [\, \vec{e}_{x_i}^1 \quad \vec{e}_{y_i}^1 \quad \vec{e}_{z_i}^1 \,]^T$ of beam A_iB_i in terms of the reference frame $\vec{\mathbf{e}}^0$

$$\vec{\mathbf{e}}_i^1 = \begin{bmatrix} \cos\beta & 0 & \sin\beta \\ 0 & 1 & 0 \\ -\sin\beta & 0 & \cos\beta \end{bmatrix} \begin{bmatrix} \cos\alpha_i & \sin\alpha_i & 0 \\ -\sin\alpha_i & \cos\alpha_i & 0 \\ 0 & 0 & 1 \end{bmatrix} \vec{\mathbf{e}}^0 =: \mathbf{A}^1(\beta)\mathbf{A}^0(\alpha_i)\vec{\mathbf{e}}^0 \tag{2}$$

The position vector of node B_i is defined by

$$\vec{r}_{B_i} = \vec{r}_{A_i} + [\, L(t) \quad 0 \quad 0\,]\vec{\mathbf{e}}_i^1 \tag{3}$$

where $L(t)$ is the distance between nodes A_i and B_i. This distance changes if buckling of beams A_iB_i occurs. Note that Eqs. (1) and (3) define the position vectors of all nodes A_i and B_i, which can be conveniently used to compute the tendon lengths. Expressions of the cross tendon length $l_c(t)$, e.g. of the tendon located between nodes A_2 and B_1, and the horizontal tendon length $l_h(t)$, e.g. of the tendon located between nodes B_2 and B_1, are then found to be

$$l_c = \sqrt{L^2(t) + 2\sqrt{3}a_1 L(t)\sin(\alpha_{02} - \alpha)\cos\beta + 3a_1^2} \tag{4}$$

$$l_h = \sqrt{3L^2(t)\cos^2\beta + 6a_1 L(t)\cos\alpha\cos\beta + 3a_1^2} \tag{5}$$

For the model, due to symmetry, it is sufficient to consider the position of strut B_1C_1 solely. Therefore, two other rotations, $\theta_1(t) = \theta_{01} + \theta(t)$ (defined in the horizontal plane through nodes B_i) and $\varphi(t)$ (defined in the plane through nodes B_1 and C_1 perpendicular to the horizontal plane) are defined to express the body-fixed reference frame $\vec{\mathbf{e}}_1^2 = [\, \vec{e}_{x_1}^2 \quad \vec{e}_{y_1}^2 \quad \vec{e}_{z_1}^2 \,]^T$ of strut B_1C_1 in terms of the reference frame $\vec{\mathbf{e}}^0$

$$\vec{\mathbf{e}}_1^2 = \mathbf{A}^1(\varphi)\mathbf{A}^0(\theta_1)\vec{\mathbf{e}}^0 \tag{6}$$

Here, again the direction cosine matrices of Eq. (2) are used, but now based on θ_1 and φ. The position vectors of the center of mass of strut B_1C_1, the top mass, and node C_1 are respectively defined by

$$\vec{r}_{cm_2} = [x_2(t) \;\; y_2(t) \;\; u(t) + z_2(t)]\vec{\mathbf{e}}^0 \tag{7}$$

$$\vec{r}_{cm_3} = [0 \;\; 0 \;\; u(t) + z_3(t)]\vec{\mathbf{e}}^0 \tag{8}$$

$$\vec{r}_{C_1} = [a_3\cos\theta_1 \;\; a_3\sin\theta_1 \;\; u(t) + z_3(t)]\vec{\mathbf{e}}^0 \tag{9}$$

3. Buckling modeling

Fig. 2 shows the perfect and buckled geometry of beam A_1B_1 and the Cartesian reference frame $\vec{\mathbf{e}}_1^1$. The origin of this reference frame coincides with node A_1.

The axial displacement field $l_a(t,x_1)$ of beam A_1B_1 is defined in the $\vec{e}_{x_1}^1$-direction and the transversal displacement field $h_a(t,x_1)$ in the $\vec{e}_{z_1}^1$-direction. Coordinate x_1 is the beam centerline coordinate. The displacement field in $\vec{e}_{y_1}^1$-direction is neglected due to $H \ll W$. It is assumed that the centerline of beam A_1B_1 initially has a geometrical shape imperfection $h_{a0}(x_1)$. Note that due to the assumption of symmetry, it is also assumed that all imperfections in beams A_iB_i are identical. The centerline of beam A_1B_1 is described by the curve $X(t,x_1)\vec{e}_{x_1}^1 + Z(t,x_1)\vec{e}_{z_1}^1$, where

$$X(t,x_1) = x_1 + l_a(t,x_1) \tag{10a}$$

$$Z(t,x_1) = h_{a0}(x_1) + h_a(t,x_1) \tag{10b}$$

The transversal displacement field is discretized based on the *Assumed-Mode Method* (Tongue, 1996) by using separation of variables using a time varying amplitude $h(t)$ and a shape function $\phi(x_1)$

$$h_a(t,x_1) = h(t)\phi(x_1) \tag{11}$$

The initial geometrical shape imperfection of beam A_1B_1 is discretized in an analogous way

$$h_{a0}(x_1) = h_0\phi(x_1) \tag{12}$$

It is assumed that beams A_iB_i are pinned–pinned at nodes A_i and B_i. Consequently, the transversal displacement and the reaction moments at the beam's ends are zero, i.e. $h_a(t,0) = h_a(t,L_1) = 0$ and $\partial^2 h_a(t,0)/\partial x_1^2 = \partial^2 h_a(t,L_1)/\partial x_1^2 = 0$. Now, the following shape function is admissible because it obeys the latter kinematic and dynamic boundary conditions and it can be differentiated infinitely many times

$$\phi(x_1) = \sin\left(\frac{\pi x_1}{L_1}\right) \tag{13}$$

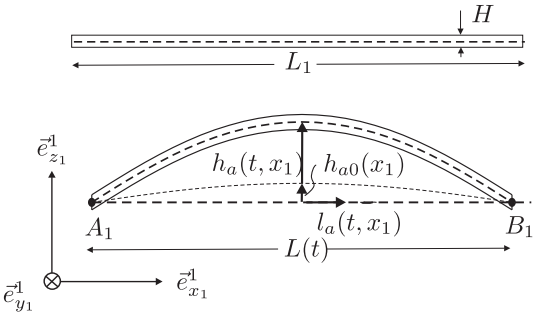

Fig. 2. Geometrical description of perfect beam A_1B_1 (upper figure) and the bucked beam A_1B_1 (lower figure).

Axially, the beam is assumed to be inextensible. The axial displacement field $l_a(t,x_1)$ is kinematically related to the transversal displacement field $h_a(t,x_1)$ by the inextensibility constraint

$$\frac{\partial l_a}{\partial x_1}(t,x_1) = \sqrt{1 - 2\frac{\partial h_{a0}}{\partial x_1}\frac{\partial h_a}{\partial x_1} - \left(\frac{\partial h_a}{\partial x_1}\right)^2} - 1 \tag{14}$$

see e.g. Koiter (1945) and Fey et al. (2011). The axial displacement field is obtained by integrating Eq. (14)

$$l_a(t,x_1) = \int_0^{x_1} \frac{\partial l_a(t,x_1')}{\partial x_1'}\,\mathrm{d}x_1' \tag{15}$$

The expressions of the axial and transversal displacement field, together with the angles α and β, fully define the position vector of a point of beam A_1B_1 in terms of the reference frame $\vec{\mathbf{e}}^0$

$$\vec{r}_1(x_1,y_1,z_1,t) = \vec{r}_{A_1} + \begin{bmatrix} x_1 + l_a(t,x_1) \\ y_1 \\ z_1 + h_{a0}(x_1) + h_a(t,x_1) \end{bmatrix}^T \mathbf{A}^1(\beta)\mathbf{A}^0(\alpha_1)\vec{\mathbf{e}}^0 \tag{16}$$

The latter expression is valid for $0 \leqslant x_1 \leqslant L_1$, $-W/2 \leqslant y_1 \leqslant W/2$, and $-H/2 \leqslant z_1 \leqslant H/2$. The distance between nodes A_i and B_i, used in Eq. (3), is equal to

$$L(t) = L_1 + l_a(t,L_1) \tag{17}$$

The material type of beams A_iB_i is assumed to be linearly elastic. The exact curvature $\kappa(t,x_1)$ of beam A_1B_1 follows from Koiter (1945)

$$\kappa(t,x_1) = \frac{(\partial X/\partial x_1)(\partial^2 Z/\partial x_1^2) - (\partial^2 X/\partial x_1^2)(\partial Z/\partial x_1)}{\left((\partial X/\partial x_1)^2 + (\partial Z/\partial x_1)^2\right)^{\frac{3}{2}}} \tag{18}$$

It is important to note that 5th-order Taylor series expansions are used to approximate Eqs. (14) and (18) because these expressions can not be integrated symbolically as will be necessary later on to derive the energy functions of the system. Note further that, in absence of geometrical imperfections and transversal loading, i.e. when there is no gravity, static buckling of beams A_iB_i occurs if the critical axial Euler buckling load P_c is exceeded, where

$$P_c = \frac{\pi^2 EI}{L_1^2} \quad \text{with } I = \frac{1}{12}WH^3. \tag{19}$$

4. Equations of motion

Due to the complexity induced by the 3D geometry and by buckling modeling, the equations of motion are first conveniently derived for a set of nine dependent DOFs in Section 4.1. Due to symmetry, only one third of the structure will be taken into account in the energy expressions. In Section 4.2, the equations of motion are reduced to a formulation of the dynamics in terms of a set of three independent DOFs.

4.1. Constrained equations of motion

The equations of motion are derived by applying Lagrange's equation of motion with constraints

$$\begin{cases} \frac{\mathrm{d}}{\mathrm{d}t}(\mathcal{T}_{,\dot{\mathbf{q}}}) - \mathcal{T}_{,\mathbf{q}} + \mathcal{V}_{,\mathbf{q}} = -\mathcal{R}_{,\dot{\mathbf{q}}} + (\mathbf{W}\boldsymbol{\lambda})^T \\ \mathbf{W}^T\dot{\mathbf{q}} = \mathbf{0} \end{cases} \tag{20}$$

where $\mathbf{q}$ is a column containing the nine dependent DOFs, which describe the deformed geometry of the (symmetric) tensegrity structure, i.e.

$$\mathbf{q} = [\,\alpha \quad \beta \quad h \quad x_2 \quad y_2 \quad z_2 \quad \theta \quad \varphi \quad z_3\,]^T \tag{21}$$

In Eq. (20), $\mathcal{V}$ is the total potential energy function, $\mathcal{T}$ is the total kinetic energy function, $\mathcal{R}$ is a Rayleigh dissipation function, and λ is a column with Lagrange's multipliers, which are related to the forces and torques working on the system to ensure the satisfaction of the kinematic constraint equations, on velocity level represented by $\mathbf{W}^T\dot{\mathbf{q}} = \mathbf{0}$.

4.1.1. Energy functions

The total potential energy function $\mathcal{V}$ is the sum of the axial strain energy of one cross tendon $\mathcal{V}_{\epsilon,c}$, one horizontal tendon $\mathcal{V}_{\epsilon,h}$, the gravitational energy $\mathcal{V}_g$, and the bending strain energy $\mathcal{V}_b$ of beam A_1B_1

$$\mathcal{V} = \mathcal{V}_{\epsilon,c} + \mathcal{V}_{\epsilon,h} + \mathcal{V}_g + \mathcal{V}_b \tag{22}$$

The tendons are modeled as piecewise linear springs, which can only take tensile forces. Therefore, the axial strain energy function $\mathcal{V}_{\epsilon,i}$ of tendon i (i=c,h) becomes

$$\mathcal{V}_{\epsilon,i} = \begin{cases} 0 & \text{if } l_i(t) - l_{0i} < 0 \\ \frac{1}{2}k_i(l_i - l_{0i})^2 & \text{if } l_i(t) - l_{0i} > 0 \end{cases} \tag{23}$$

where $l_i(t)$ is the time-dependent tendon length, see Eqs. (4) and (5), l_{0i} is the stress-free tendon length, and k_i is the tendon stiffness. The total gravitational energy function $\mathcal{V}_g$ is based on the mass of beam A_1B_1, strut B_1C_1, and one third of the top mass

$$\mathcal{V}_g = \rho_1 g \iiint_V \vec{r}_1(x_1,y_1,z_1,t)\cdot\vec{e}_z^0\,\mathrm{d}x_1\,\mathrm{d}y_1\,\mathrm{d}z_1 + m_2 g(u(t)+z_2) + \frac{1}{3}m_3 g(u(t)+z_3) \tag{24}$$

where $V = [(x_1,y_1,z_1) \in \mathbb{R}^3 | 0 \leqslant x_1 \leqslant L_1, -W/2 \leqslant y_1 \leqslant W/2, -H/2 \leqslant z_1 \leqslant H/2]$ specifies the volume of beam A_1B_1, $m_2 = \pi\rho_2 L_2 R^2$ is the mass of strut B_1C_1, and g is the gravitation acceleration constant. Note that the mass of beam A_1B_1 is equal to $m_1 = \rho_1 L_1 H\,W$. The strain energy due to bending of beam A_1B_1 follows from

$$\mathcal{V}_b = \frac{E_1 I_1}{2}\int_0^{L_1}(\kappa-\kappa_0)^2\,\mathrm{d}x_1 = \frac{P_c L_1^2}{2\pi^2}\int_0^{L_1}(\kappa-\kappa_0)^2\,\mathrm{d}x_1 \tag{25}$$

where κ_0 describes the curvature of beam A_1B_1 in the strain-free situation due to the geometrical imperfection $h_{a0}(x_1)$. As mentioned before, the latter integral is solved by taking 5th-order Taylor series approximations of the beam curvature κ, see also Eq. (18).

The total kinetic energy function $\mathcal{T}$ is the sum of the kinetic energy $\mathcal{T}_{m_1}$ of beam A_1B_1, the kinetic energy $\mathcal{T}_{m_2}$ of strut B_1C_1, and the kinetic energy $\mathcal{T}_{m_3}$ of one third of the top mass

$$\mathcal{T} = \mathcal{T}_{m_1} + \mathcal{T}_{m_2} + \mathcal{T}_{m_3} \tag{26}$$

The kinetic energy function of beam A_1B_1 includes the translational and rotational energy of the beam and is computed by solving

$$\mathcal{T}_{m_1} = \frac{1}{2}\rho_1 \iiint_V \dot{\vec{r}}_1\cdot\dot{\vec{r}}_1\,\mathrm{d}x_1\,\mathrm{d}y_1\,\mathrm{d}z_1 \tag{27}$$

where V is as specified above. The kinetic energy function of strut B_1C_1 equals

$$\mathcal{T}_{m_2} = \tfrac{1}{2}m_2(\dot{\vec{r}}_{cm_2}\cdot\dot{\vec{r}}_{cm_2}) + \tfrac{1}{2}\vec{\boldsymbol{\omega}}\cdot\left(\vec{\mathbf{e}}_1^{2^T}\mathbf{J}_{cm_2}\vec{\mathbf{e}}_1^2\right)\cdot\vec{\omega} \tag{28}$$

where $\vec{\boldsymbol{\omega}}$ is the angular velocity vector, which is expressed in terms of the body fixed reference frame $\vec{\mathbf{e}}_1^2$ by using the direction-cosine matrices of Eq. (6)

$$\vec{\omega} = [\,0 \quad \dot{\varphi} \quad 0\,]\vec{\mathbf{e}}_1^2 + [\,0 \quad 0 \quad \dot{\theta}_1\,]\mathbf{A}^{1^T}(\varphi)\vec{\mathbf{e}}_1^2 \tag{29}$$

and $\vec{\mathbf{e}}_1^{2^T}\mathbf{J}_{cm_2}\vec{\mathbf{e}}_1^2$ is the inertia tensor of strut B_1C_1. For the cylindrically shaped strut B_1C_1, the diagonal elements of the diagonal inertia matrix $\mathbf{J}_{cm_2}$ are equal to $J_{x_2x_2} = \frac{1}{2}m_2R^2$ and $J_{y_2y_2} = J_{z_2z_2} = \frac{1}{2}m_2(3R^2 + L_2^2)$. Substituting the first time derivative of Eq. (7) and the angular

velocity vector of Eq. (29) in Eq. (28) leads to the kinetic energy function of strut B_1C_1

$$\mathcal{T}_{m_2} = \tfrac{1}{2}m_2\left(\dot{x}_2^2 + \dot{y}_2^2 + \dot{z}_2^2 + \dot{u}(t)^2 + 2\dot{u}(t)\dot{z}_2\right) + \tfrac{1}{2}(J_{x_2x_2}\sin^2\varphi + J_{z_2z_2}\cos^2\theta)\dot{\theta}^2 + \tfrac{1}{2}J_{y_2y_2}\dot{\varphi}^2 \quad (30)$$

The kinetic energy of one third of the top mass, which is assumed to be only translating in vertical direction, is equal to

$$\mathcal{T}_{m_3} = \tfrac{1}{6}m_3\left(\dot{z}_3^2 + \dot{u}(t)^2 + 2\dot{u}(t)\dot{z}_3\right) \quad (31)$$

The generalized damping forces, based on a linear viscous damping model, are taken into account by the Rayleigh dissipation function

$$\mathcal{R} = \tfrac{1}{2}(c_{11}\dot{\alpha}^2 + c_{22}\dot{\beta}^2 + c_{33}\dot{h}^2) + c_{12}\dot{\alpha}\dot{\beta} + c_{13}\dot{\alpha}\dot{h} + c_{23}\dot{\beta}\dot{h} \quad (32)$$

Note that only time derivatives of DOFs α, β, and h play a role in Eq. (32), because these DOFs will be chosen as the three independent DOFs in Section 4.2.

4.1.2. Constraint equations

The kinematic constraint equations relate the dependent DOFs x_2, y_2, z_2, θ, φ, and z_3 to the independent DOFs α, β, and h. The first three kinematic constraint equations follow by equating Eq. (7) to the following expression for the position vector of the center of mass of strut B_1C_1

$$\vec{r}_{cm_2} = \vec{r}_{A_1} + [L \quad 0 \quad 0]\vec{\mathbf{e}}_1^1 + \tfrac{1}{2}[L_2 \quad 0 \quad 0]\vec{\mathbf{e}}_1^2 \quad (33)$$

The final three kinematic constraint equations are found by equating two expressions for the position vector $\vec{r}_{C_1}$ of node C_1,

$$\vec{r}_{A_1} + [L \quad 0 \quad 0]\vec{\mathbf{e}}_1^1 + [L_2 \quad 0 \quad 0]\vec{\mathbf{e}}_1^2 = [a_3\cos\theta \quad a_3\sin\theta \quad u(t) + z_3]\vec{\mathbf{e}}^0 \quad (34)$$

Working out Eqs. (33) and (34) results in six holonomic, scleronomic kinematic constraint equations

$$\mathbf{h}_c = \begin{bmatrix} x_2 - L\cos\alpha\cos\beta - \frac{1}{2}L_2\cos\theta\cos\varphi \\ y_2 - L\sin\alpha\cos\beta - \frac{1}{2}L_2\sin\theta\cos\varphi \\ z_2 - L\sin\beta - \frac{1}{2}L_2\sin\varphi \\ \theta - \arctan Z_1 \\ \varphi - \arccos Z_2 \\ z_3 - L\sin\beta - L_2\sin\varphi \end{bmatrix} = \mathbf{0} \quad (35)$$

with $Z_1 = (L\sin\alpha\cos\beta)/(a_1 + L\cos\alpha\cos\beta)$ and $Z_2 = (a_3 - \sqrt{L^2\cos^2\beta + 2a_1L\cos\alpha\cos\beta + a_1^2})/L_2$.

Substitution of Eqs. (22), (26), and (32) in Eq. (20) results in the equations of motion and a set of constraint equations

$$\begin{cases} \overline{\mathbf{M}}(\mathbf{q})\ddot{\mathbf{q}} + \overline{\mathbf{G}}(\dot{\mathbf{q}},\mathbf{q}) + \overline{\mathbf{C}}\dot{\mathbf{q}} + \overline{\mathbf{H}}(\mathbf{q}) = \overline{\mathbf{B}}(\mathbf{q})\ddot{u}(t) + (\mathbf{W}\lambda)^T \\ \mathbf{W}^T\dot{\mathbf{q}} = \mathbf{0} \end{cases} \quad (36)$$

where the holonomic constraint equations of Eq. (35) are written on velocity level by

$$\dot{\mathbf{h}}_c = \mathbf{W}^T\dot{\mathbf{q}} = \mathbf{0} \quad \text{with} \quad \mathbf{W}^T(\mathbf{q}) = \frac{\partial\mathbf{h}_c(\mathbf{q})}{\partial\mathbf{q}} \quad (37)$$

4.2. Unconstrained equations of motion

The equations of motion with constraints, i.e. Eq. (36), are reduced to a formulation of the dynamics in terms of independent DOFs. In this formulation, the explicit use of the constraint equations, and thus the Lagrange's multipliers λ, is avoided. As mentioned before, the tensegrity structure configuration is fully defined by α, β, and h, implying a set of independent DOFs

$$\mathbf{q}_m = [\alpha \quad \beta \quad h]^T \quad (38)$$

The constraint equations of Eq. (35) establishes the relation between the dependent DOFs $\mathbf{q}$, see Eq. (21), and the independent DOFs $\mathbf{q}_m$ by $\mathbf{q} = \mathbf{q}(\mathbf{q}_m(t))$. The velocity and acceleration of the dependent DOFs in terms of the independent DOFs are $\dot{\mathbf{q}} = \mathbf{T}(\mathbf{q}_m(t))\dot{\mathbf{q}}_m$ and $\ddot{\mathbf{q}} = \mathbf{T}(\mathbf{q}_m(t))\ddot{\mathbf{q}}_m + \dot{\mathbf{T}}(\dot{\mathbf{q}}_m(t),\mathbf{q}_m(t))\dot{\mathbf{q}}_m$ respectively, where $\mathbf{T}(\mathbf{q}_m(t)) = \partial\mathbf{q}(\mathbf{q}_m(t))/\partial\mathbf{q}_m$. Now, the equations of motion with constraints, i.e. Eq. (36), can be reduced to a formulation of the dynamics in terms of the independent DOFs, see e.g. Skelton and de Oliveira (2009)

$$\mathbf{M}(\mathbf{q}_m)\ddot{\mathbf{q}}_m + \mathbf{G}(\dot{\mathbf{q}}_m,\mathbf{q}_m) + \mathbf{C}\dot{\mathbf{q}}_m + \mathbf{H}(\mathbf{q}_m) = \mathbf{B}(\mathbf{q}_m)\ddot{u}(t) \quad (39)$$

where $\mathbf{M} = \mathbf{T}^T\overline{\mathbf{M}}\mathbf{T}, \mathbf{G} = \mathbf{T}^T\overline{\mathbf{M}}\dot{\mathbf{T}}\dot{\mathbf{q}}_m + \mathbf{T}^T\overline{\mathbf{G}}, \mathbf{C} = \mathbf{T}^T\overline{\mathbf{C}}\mathbf{T}, \mathbf{H} = \mathbf{T}^T\overline{\mathbf{H}}$, and $\mathbf{B} = \mathbf{T}^T\overline{\mathbf{B}}$.

Later on, unless stated otherwise, results are presented for the following output variables: (1) rotation $\alpha(t)$, (2) the transversal displacement measured halfway the central axis of beams A_iB_i, i.e. $h_{mid}(t) = Z(t, L_1/2)$, see Eqs. (10b) and (3) the height difference between the base (horizontal plane through nodes A_i) and the horizontal plane through nodes C_i, denoted by $h_z = \vec{r}_{C_1}(t)\cdot\vec{\mathbf{e}}_z^0 - u(t)$.

5. Geometrical and material properties

The parameter values of the undamped tensegrity structure are presented in Table 1. The corresponding critical axial buckling load of the steel beams A_iB_i follows from Eq. (19) and is equal to $P_c = 66.3$ N for $h_0 = 0$ mm. Parameter $\Delta\tilde{l}_{oc}$ will be introduced later. As stated before, all results presented later on are based on 5th-order Taylor series approximations of the inextensibility constraint, Eq. (14), and the beam curvature, Eq. (18). In this way, accurate results are obtained in the displacement range of interest, while keeping computation times acceptable.

It is assumed that the stiffness of the tendons is so high, that the elongation of the tendons will always remain small compared to their lengths. Therefore, initially, the stress-free tendon lengths are computed by using an imaginary reference configuration $\mathbf{q}_m^0$, in which buckling, beam imperfections, gravity, and elongation of the horizontal tendons are neglected, i.e. $L(t) = L_1$, $h_0 = 0$, $g = 0$, and the position of nodes B_i in the horizontal plane is known and located on a circle with radius a_2. In this case, the total potential energy function only contains the strain energy of the cross tendons. The cross tendon length l_c is now described by one DOF, namely α. Minimizing this energy function to zero and taking into account the geometrical boundary conditions, i.e. beams A_iB_i and cross tendons should not interfere, results in the imaginary reference configuration $\mathbf{q}_m^0$. For chosen values of a_1, a_2 (see Fig. 1), and L_1 this leads to

$$\mathbf{q}_m^0 = \begin{bmatrix} \frac{11}{12}\pi \\ \arcsin\frac{1}{L_1}\left(L_1^2 - \sqrt{3}a_1a_2 - \left(a_1^2 + a_2^2\right)\right)^{\frac{1}{2}} \\ 0 \end{bmatrix} \quad (40)$$

For this (imaginary) reference configuration, the corresponding stress-free tendon lengths $\tilde{l}_{oc}$ and l_{oh} are found by substituting

Table 1
Parameters values of the tensegrity structure.

Parameter	Value	Unit	Parameter	Value	Unit
a_1	8.75	cm	L_1	30.0	cm
a_2	8.75	cm	W	2.0	cm
a_3	1.50	cm	H	1.2	mm
g	9.81	m/s^2	ρ_1	7850	kg/m^3
k_c	1.403×10^5	N/m	E_1	2.1×10^{11}	N/m^2
$\Delta\tilde{l}_{oc}$	3.56×10^{-5}	m	P_c	66.3	N
l_{oc}	25.195	cm	h_0	−1.0	mm
k_h	2.332×10^5	N/m	L_2	10.0	cm
l_{oh}	15.155	cm	R	7.5	mm
ρ_2	2700	kg/m^3			

Eq. (40) in Eqs. (4) and (5) respectively. In the static equilibrium position of the unloaded system ($m_3 = 0$ and $u(t) = 0$), a small level of prestress in the tendons is desired and a substantial amount of compressive stress in the beams is required to be near the static stability boundary of the system. Therefore, in the actual model, the real stress-free cross tendon length l_{oc} is specified by shortening $\tilde{l}_{oc}$ by choosing $\Delta\tilde{l}_{oc} = 3.56 \times 10^{-5}$ m

$$l_{oc} = \tilde{l}_{oc} - \Delta\tilde{l}_{oc} \tag{41}$$

Shortening $\tilde{l}_{oc}$ can be interpreted as a way to define a pretension in the cross tendons of $F_c^0 = k_c \Delta\tilde{l}_{oc} = 5.0$ N. Note that this pretension will increase the pretension caused by the gravity field, acting on beams A_iB_i, struts B_iC_i, and top mass m_3.

6. Static responses

The top mass is replaced by a vertical force, equal to $F_{ex} = m_3 g$, in order to compute the static load path of the system. Here, $F_{ex} > 0$ represents a downward force and consequently $F_{ex} < 0$ represents an upward force. In Fig. 3, F_c^* is the static cross tendon force, F_h^* is the static horizontal tendon force, and F_b^* is the static compressive force between nodes A_i and B_i. The latter force is computed by solving the equilibrium equations of node A_1. Fig. 3 shows that for $F_{ex} = 0$, there is pretension in the tendons and a compressive force in the beams, which are not perfectly straight due to gravity and a geometrical shape imperfection.

Fig. 4 shows the corresponding branches of stable static equilibrium points $\mathbf{q}_m^*$. Note that the stable static equilibrium points are the solutions of $\mathcal{V}_{,\mathbf{q}_m} = 0$, provided that $\mathcal{V}_{,\mathbf{q}_m\mathbf{q}_m}(\mathbf{q}_m^*) > 0$. Static buckling of beams A_iB_i becomes more dominant when increasing the compressive load F_{ex} or m_3. In a tensile test ($F_{ex} < 0$), slackening of the horizontal tendons occurs at $F_{ex} = -54.94$ N. Thus, below this value, indicated by a circle '$\circ$', structural integrity is lost. Slackening of the horizontal tendons is further illustrated by looking at the horizontal tendon force F_h^*, which becomes zero at $F_{ex} = -54.94$ N, see Fig. 3. All internal equilibrium forces have a minimum (in an absolute sense) at $F_{ex} = -2.26$ N. Here, gravity, acting on beams A_iB_i and struts B_iC_i, and the pretension of the cross tendons due to $\Delta\tilde{l}_{oc}$ is canceled out to some extent by the external tensile load. For the tensile test, the horizontal tendon force F_h^* has a maximum at $F_{ex} = -17.66$ N, whereas, for the compressive test, the cross tendon force F_c^* shows a maximum at $F_{ex} = 44.16$ N.

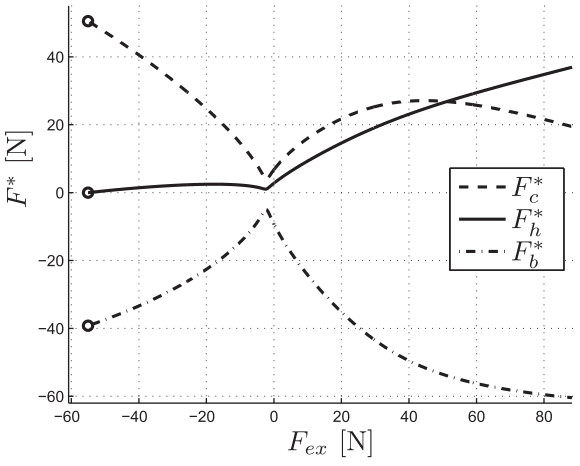

Fig. 3. The internal equilibrium forces for varying external loads ($F_{ex} = m_3 g$).

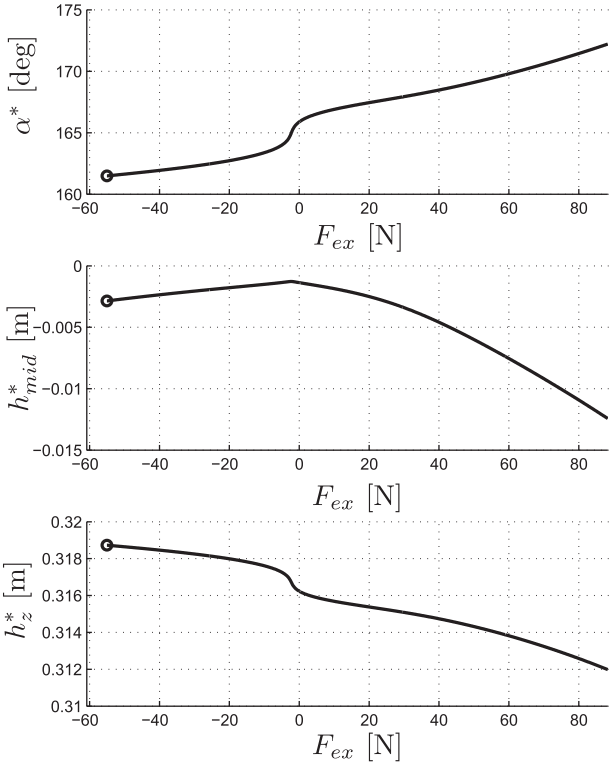

Fig. 4. The stable static equilibrium points for varying external loads ($F_{ex} = m_3 g$).

7. Modal analysis

The nonlinear equations of motion of Eq. (39) are linearized around a stable static equilibrium point $\mathbf{q}_m^*$ for modal analysis and to compute FRFs of the system. Throughout this paper, (small) dynamical responses of the linearized equations of motion are denoted by $\Delta\mathbf{q}_m$.

7.1. Undamped eigenfrequencies

The system's undamped eigenvalues $\lambda_{0k} = \pm j\omega_{0k}$ ($j^2 = -1$) and corresponding eigenmodes $\mathbf{u}_{0k}$ are found by solving the eigenvalue problem

$$(\mathbf{H}_l - \omega_{0k}^2 \mathbf{M}_l)\mathbf{u}_{0k} = \mathbf{0} \tag{42}$$

where $\mathbf{M}_l$ and $\mathbf{H}_l$ are respectively the mass and stiffness matrix of the linearized equations of motion, $\omega_{0k} = 2\pi f_{0k}$ is the kth undamped angular eigenfrequency, and $\mathbf{u}_{0k} = [\,u_{1k} \quad u_{2k} \quad u_{3k}\,]^T$ is the corresponding kth (real) eigenmode. The resulting undamped eigenfrequencies f_{0k} are shown in Fig. 5 for a varying top mass m_3. The first undamped eigenfrequency f_{01} shows a maximum at $m_3 = 1.5$ kg. The second undamped eigenfrequency f_{02} starts to increase when static buckling becomes significant and the third undamped eigenfrequency f_{03} shows a minimum at $m_3 = 4.8$ kg.

From this point on, the top mass is fixed to $m_3 = 3.0$ kg, which corresponds to $F_{ex} = 29.4$ N in Section 6. For this choice, all tendons are clearly under tension and still no severe static buckling occurs in the stable static equilibrium configuration.

7.2. Undamped eigenmodes

The kth undamped eigenmode $\mathbf{u}_{0k}$ is normalized with respect to the spatial position of node B_1 evaluated at the stable static equilibrium point $\mathbf{q}_m^*$ corresponding to a top mass of $m_3 = 3.0$ kg. The kth eigenmode, denoted by $\delta\mathbf{u}_{0k} = [\,\delta\alpha_k \quad \delta\beta_k \quad \delta h_k\,]^T$, is normalized

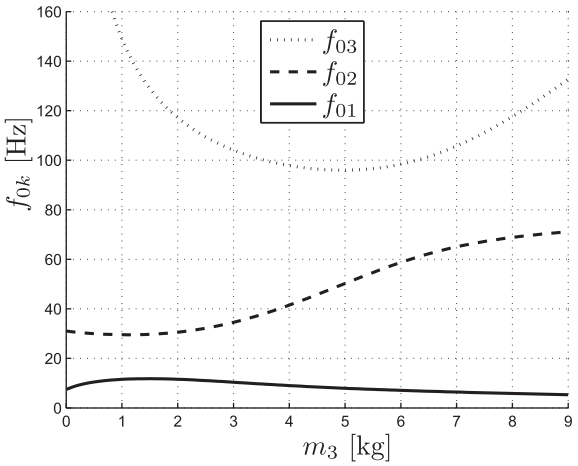

Fig. 5. The undamped eigenfrequencies for a varying top mass.

Table 2
The undamped eigenfrequencies and the corresponding normalized eigenmodes for $m_3 = 3.0$ kg.

f (Hz)		$\delta\mathbf{u}_{01}$	$\delta\mathbf{u}_{02}$	$\delta\mathbf{u}_{03}$
$f_{01} = 10.4$	$\delta\alpha$	0.1105	−0.0949	0.1168
$f_{02} = 34.5$	$\delta\beta$	−0.0185	0.0115	0.0012
$f_{03} = 104.1$	δh	−0.0139	−0.0342	−0.0094

in such a way that the absolute displacement with respect to $\vec{r}_{B_1}(\mathbf{q}_m^*(m_3 = 3))$ is equal to $\Delta r = 2.0$ cm by

$$\left|\vec{r}_{B_1}(\mathbf{q}_m^*) - \vec{r}_{B_1}(\mathbf{q}_m^* - \delta\mathbf{u}_{0k})\right| = \Delta r \tag{43}$$

Fig. 6 shows the resulting normalized eigenmodes $\delta\mathbf{u}_{0k}$, corresponding to the undamped eigenfrequencies f_{0k}. The values of the undamped eigenfrequencies and normalized eigenmodes are presented in Table 2. The first normalized eigenmode $\delta\mathbf{u}_{01}$ is dominated by a rotation around the vertical axis (large $\delta\alpha$) and buckling of beams A_iB_i is most dominant in the second normalized eigenmode $\delta\mathbf{u}_{02}$ (largest δh). The first and third normalized eigenmode show similar behavior. However, the third normalized eigenmode $\delta\mathbf{u}_{03}$ is characterized by less buckling of beams A_iB_i and the sign of $\delta\beta$ is positive in contrast to a negative $\delta\beta$ value for the first normalized eigenmode. Physically, the third eigenmode can be interpreted as the normalized eigenmode, in which deformation of the horizontal tendons dominates the response.

The undamped angular eigenfrequencies $\omega_{0k} = 2\pi f_{0k}$ are stored in diagonal matrix $\mathbf{\Omega}_0$ and the corresponding eigenmodes column-wise in matrix $\mathbf{U}_0$ in order to compute the proportional damping matrix (for $m_3 = 3.0$ kg)

$$\mathbf{C} = 2\mathbf{U}_0^{-T}\left(\mathbf{U}_0^T\mathbf{M}_l\mathbf{U}_0\right)\mathbf{\Xi}\mathbf{\Omega}_0\mathbf{U}_0^{-1} \tag{44}$$

where diagonal matrix $\mathbf{\Xi}$ contains the rather arbitrarily chosen dimensionless modal damping parameters $\xi_1 = 0.02$, $\xi_2 = 0.0175$, and $\xi_3 = 0.0225$. Consequently, the modes are clearly undercritically damped.

8. Frequency response functions

The FRFs $\mathbf{H}(f)$ of the tensegrity structure follow from the state space formulation of the linearized equations of motion

$$\mathbf{H}(f) = \mathbf{C}_t(\mathbf{A}_t - j2\pi f\mathbf{I})^{-1}\mathbf{B}_t \tag{45a}$$

where $\mathbf{I}$ is the identity matrix, f is the excitation frequency, $\mathbf{A}_t$ is the system matrix, $\mathbf{B}_t$ is the input column, and $\mathbf{C}_t$ is the output matrix, i.e.

$$\mathbf{A}_t = \begin{bmatrix} \mathbf{0} & \mathbf{I} \\ -\mathbf{M}_l^{-1}\mathbf{H}_l & -\mathbf{M}_l^{-1}\mathbf{C} \end{bmatrix}, \quad \mathbf{B}_t = \begin{bmatrix} \mathbf{0} \\ \mathbf{M}_l^{-1}\mathbf{B}_l \end{bmatrix},$$
$$\mathbf{C}_t = \frac{\partial}{\partial \mathbf{q}_m}\begin{bmatrix}\alpha & h_{mid} & h_z\end{bmatrix}^T\Big|_{\mathbf{q}_m = \mathbf{q}_m^*} \tag{45b}$$

Again, the matrices of the linearized equations of motion are denoted by the subscript l.

Fig. 7 shows three FRFs of the tensegrity structure. The vertical dashed lines indicate the eigenfrequencies f_{0k}. A clear anti-resonance in $|H_{\Delta h_z \Delta\ddot{u}}|$ is located between f_{02} and f_{03}. Note that the modulus of $H_{\Delta h_z \Delta\ddot{u}}$ is only weakly influenced by the second eigenmode, in which buckling of beams A_iB_i is dominant.

9. Nonlinear steady-state analysis

In this section, the nonlinear steady-state responses of the tensegrity structure are considered for a prescribed harmonic base acceleration

$$\ddot{u}(t) = U_a \sin(2\pi f t) \tag{46}$$

where U_a is the acceleration amplitude, f is the excitation frequency, and t is the time.

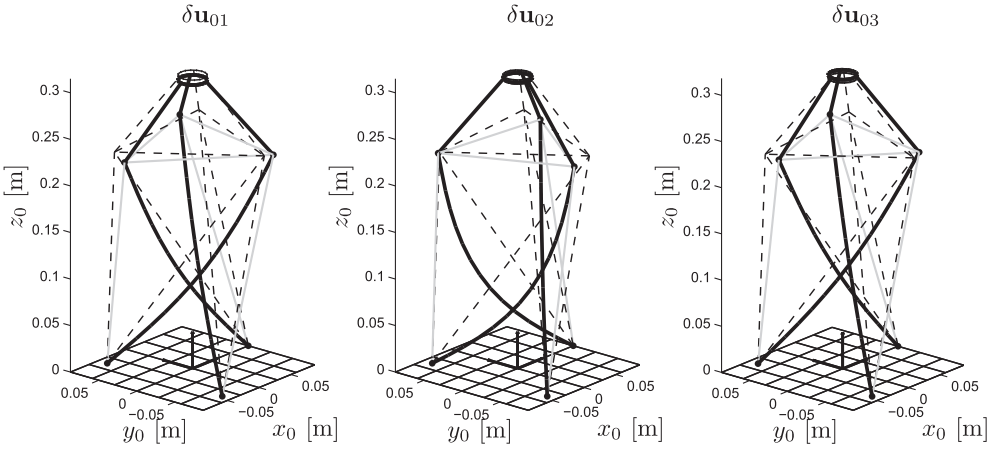

Fig. 6. Normalized eigenmodes corresponding to the undamped eigenfrequencies for $m_3 = 3.0$ kg. Dashed lines refer to the equilibrium situation.

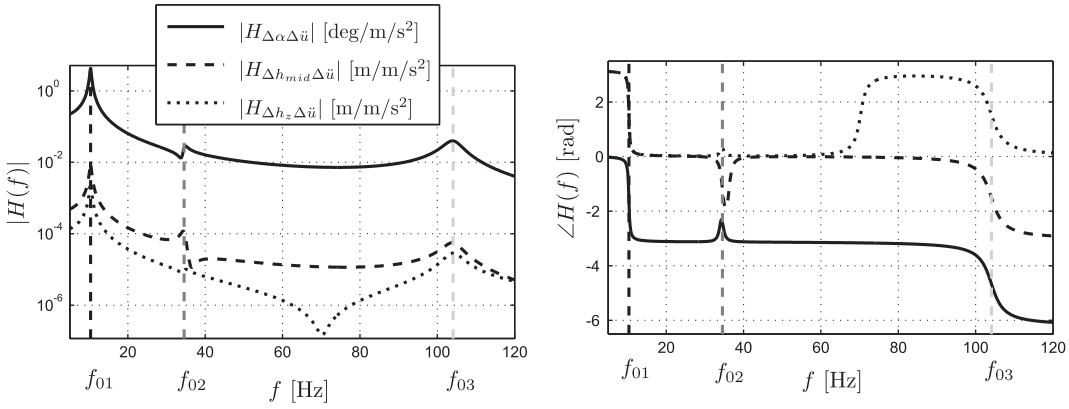

Fig. 7. Bode plot of the FRFs for $m_3 = 3.0$ kg.

9.1. Frequency-amplitude plots

Frequency-amplitude plots are computed by continuation of periodic solutions obtained by solving two point boundary value problems using the software package *AUTO97* (Doedel et al., 1998). The local stability of the periodic solutions is obtained and co-dimension one bifurcations are detected using Floquet theory, see e.g. Thomsen (2003). The amplitudes shown in the frequency-amplitude plots of Fig. 8 are the peak-to-peak values (indicated by a tilde) of the steady-state solution in terms of $\alpha(t)$, $h_{mid}(t)$, and $h_z(t)$. In addition, stable periodic solutions are depicted with solid lines, unstable periodic solutions with dashed lines, and the locations of the undamped eigenfrequencies are indicated by squares '□'. Period Doubling (PD) bifurcations will be indicated by diamonds '◇', Cyclic Fold (CF) bifurcations will be indicated by circles '○', and Secondary Hopf (SH) bifurcations, also called Neimark-Sacker bifurcations, will be indicated by triangles '△'.

Fig. 8 shows the frequency-amplitude plot in the frequency interval $2.5 \leqslant f \leqslant 117.5$ Hz for two acceleration amplitudes, namely $U_a = 1.0$ m/s^2 (black lines) and $U_a = 6.0$ m/s^2 (gray lines). Note that for $U_a = 1.0$ m/s^2, the shapes of the frequency-amplitude curves resemble the shapes of the FRFs in Fig. 7 to a large extent. Apparently, nonlinear effects play a minor role for $U_a = 1.0$ m/s^2. This especially holds for higher excitation frequencies, where response amplitudes are small. However, for $U_a = 1.0$ m/s^2, two PD bifurcations are encountered at the first harmonic resonance near $f_{01} = 10.4$ Hz, see enlargement *A*. The unstable harmonic solution branch between these PD bifurcations, located at $f = 9.82$ Hz and $f = 10.60$ Hz, shows weak softening effects, characterized by two CF bifurcations. Later on, the type of steady-state responses inside

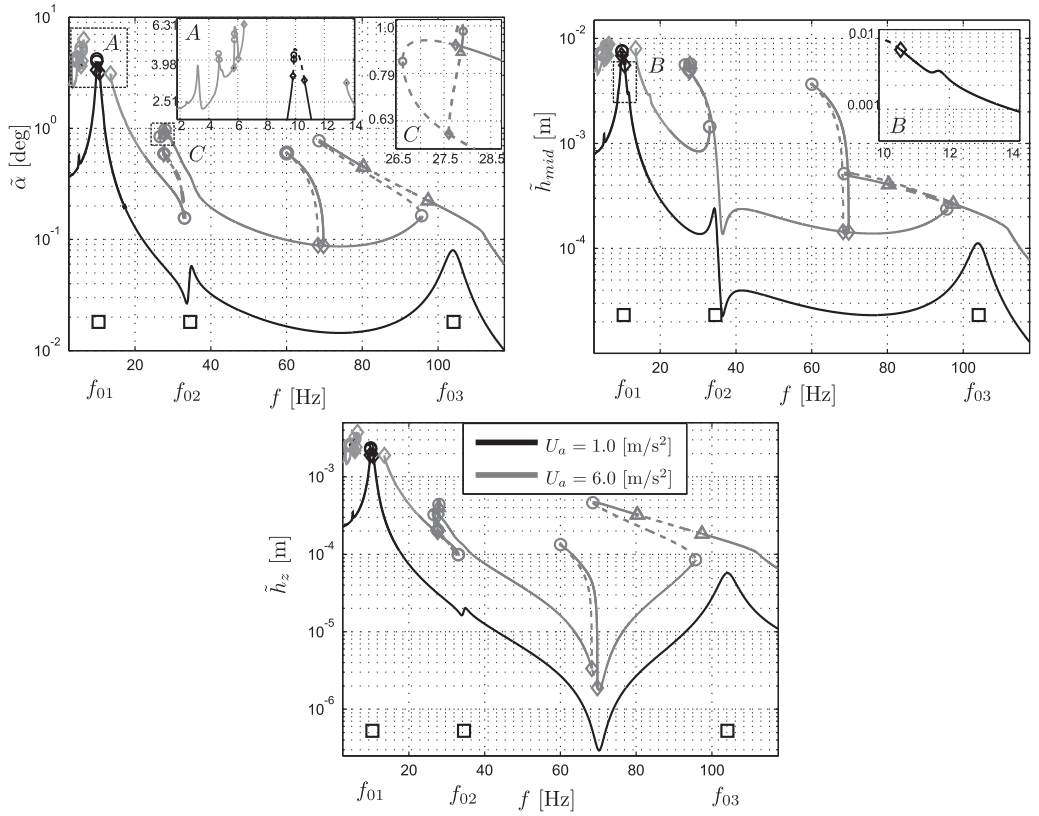

Fig. 8. Frequency-amplitude plots for $m_3 = 3.0$ kg and two acceleration amplitudes, namely $U_a = 1.0$ m/s^2 (black lines) and $U_a = 6.0$ m/s^2 (gray lines).

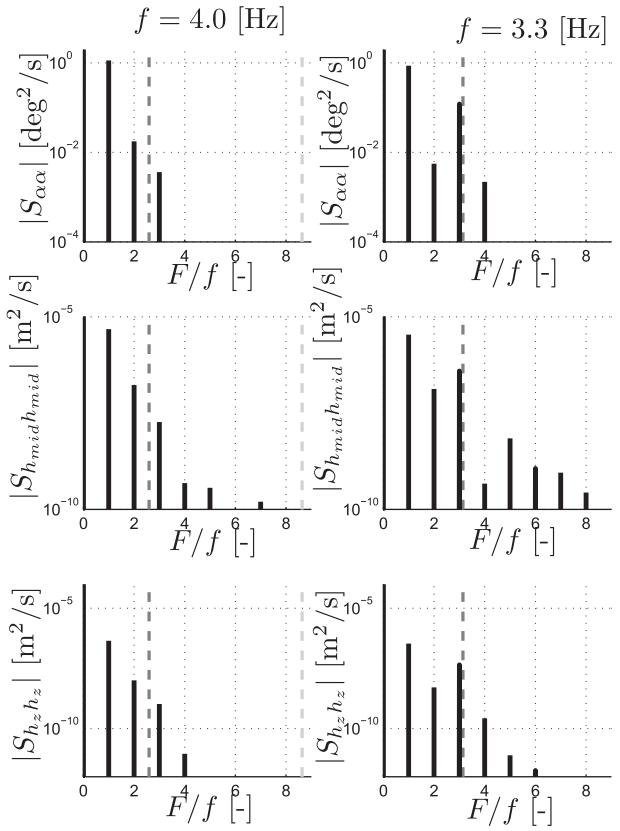

Fig. 9. PSD plots of the periodic solutions at $f = 4.0$ Hz (left plots) and $f = 3.3$ Hz (right plots) for $U_a = 6.0$ m/s^2.

the frequency interval enclosed by these PD bifurcations will be examined by constructing several Poincaré maps of steady-state solutions. Now, first, the remaining nonlinear features of the frequency-amplitude plots for $U_a = 1.0$ m/s^2 are discussed. A small second superharmonic resonance peak, corresponding to the first harmonic resonance, is observed near $f \approx f_{01}/2 = 5.2$ Hz. In addition, a small third superharmonic resonance peak is visible in the frequency-amplitude plot of $\tilde{h}_{mid}$ near $f \approx f_{02}/3 = 11.5$ Hz, see enlargement *B*. In this case, the superharmonic resonance peak is related to the second harmonic resonance.

The nonlinear dynamical behavior dramatically increases when the acceleration amplitude is set to $U_a = 6.0$ m/s^2. Near the first harmonic resonance, neither a stable nor an unstable periodic solution branch can be computed in the frequency interval enclosed by two PD bifurcations at $f = 6.5$ Hz and $f = 13.5$ Hz, see enlargement *A*. Next to the second superharmonic resonance near $f_{01}/2 = 5.2$ Hz, now showing softening behavior (indicated by two CF bifurcations), also a third superharmonic resonance near $f_{01}/3 = 3.47$ Hz and a 1/2 subharmonic resonance near $f = 2f_{01}/3$ are present in all frequency-amplitude plots but these are only clearly visible in enlargement *A*. The second harmonic resonance peak related to the second eigenfrequency at $f_{02} = 34.5$ Hz shows softening effects, which is caused by dynamic buckling of beams A_iB_i. Three stable periodic solutions coexist for the small frequency interval $27.86 \leqslant f \leqslant 27.91$ Hz, of which two are visible in enlargement *C*. Near $f = 2f_{02} = 70$ Hz a softening 1/2 subharmonic resonance related to the second eigenfrequency occurs, initiated by two PD bifurcations. Based on observations in Fey et al. (2011), this resonance is very probably due to parametric excitation. The third harmonic resonance peak near $f_{03} = 104.1$ Hz also exhibits softening behavior. In this case, softening is caused by slackening of the horizontal tendons. Finally, two SH bifurcations, located at $f = 79.92$ Hz and $f = 97.47$ Hz, are encountered on the branch related to the third harmonic resonance. Again, the steady-state solutions in the frequency interval enclosed by these SH bifurcations will be investigated later by means of Poincaré maps.

9.2. PSD plots

Now, the Power Spectral Density (PSD) plots of two nearby periodic solutions are used to study the origin of one superharmonic resonance peak in a more profound manner. The frequency F/f on the horizontal axis of the PSD plot has been normalized by the excitation frequency f. Undamped eigenfrequency f_{01} is indicated by dark-grey dashed vertical lines.

For $U_a = 6.0$ m/s^2, the PSD plots of the periodic solutions at $f = 4.0$ Hz and $f = 3.3$ Hz are presented in Fig. 9. When comparing the PSD plots of the periodic solutions at $f = 4.0$ Hz with the PSD plots of the superharmonic resonance at $f = 3.3$ Hz, for

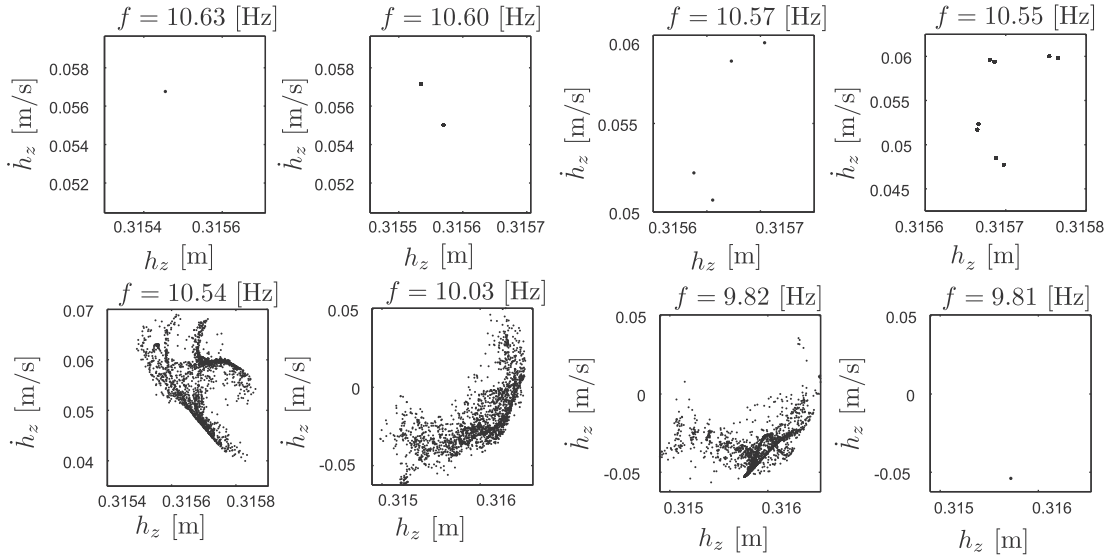

Fig. 10. Poincaré maps in the subspace spanned by h_z and $\dot{h}_z$ for different excitation frequencies f and $U_a = 1.0$ m/s^2.

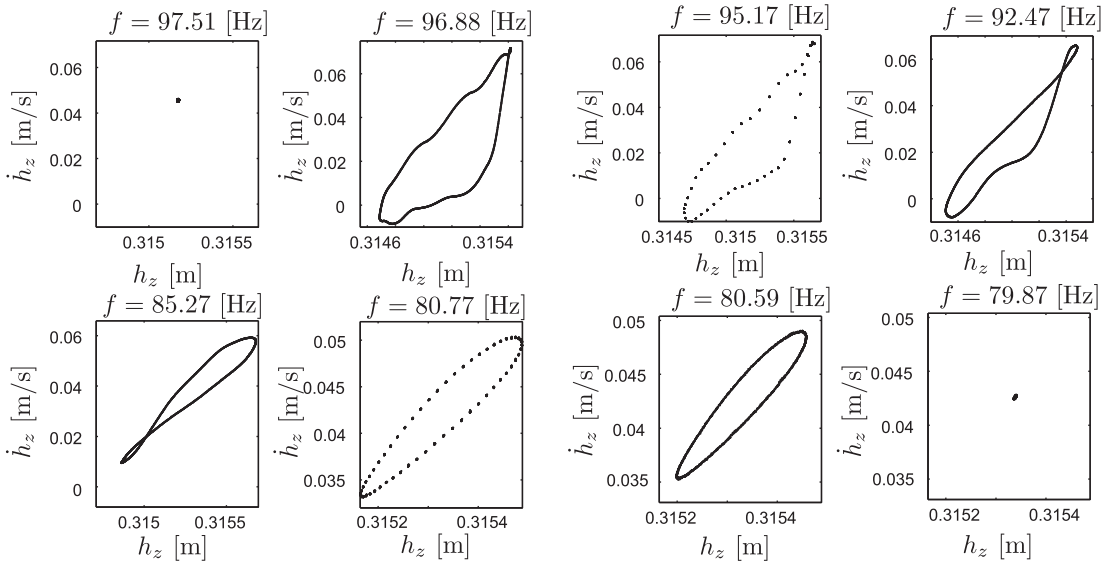

Fig. 11. Poincaré maps in the subspace spanned by h_z and $\dot{h}_z$ for different excitation frequencies f and $U_a = 6.0$ m/s^2.

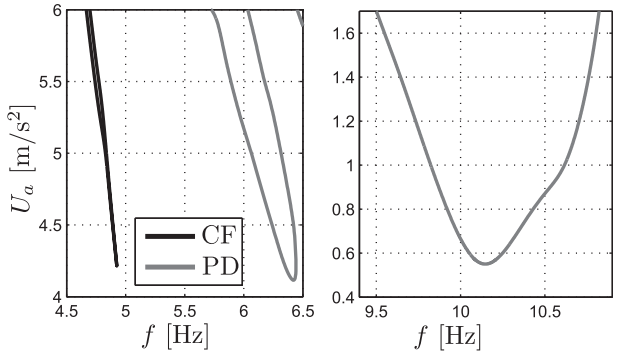

Fig. 12. Two parameter continuation diagram near the first harmonic resonance ($f_{01} = 10.4$ Hz).

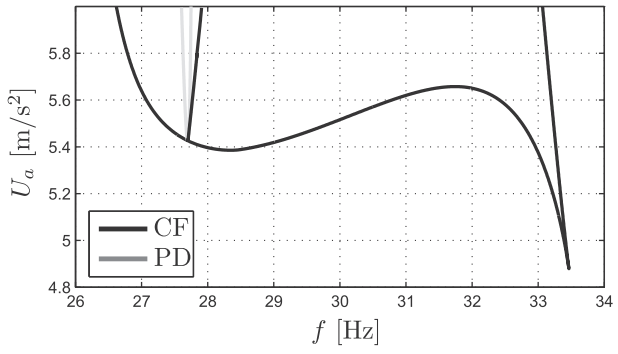

Fig. 13. Two parameter continuation diagram near the second harmonic resonance ($f_{02} = 34.5$ Hz).

the latter case a sudden increase in the magnitude can be observed at $F/f = 3$ for all responses. Indeed, $F = 3f \approx 10$ Hz approximately coincides with the first undamped eigenfrequency f_{01}. Consequently, this is a third superharmonic resonance peak, related to the first eigenfrequency. Using this approach, the origin of the remaining superharmonic resonance peaks is also validated.

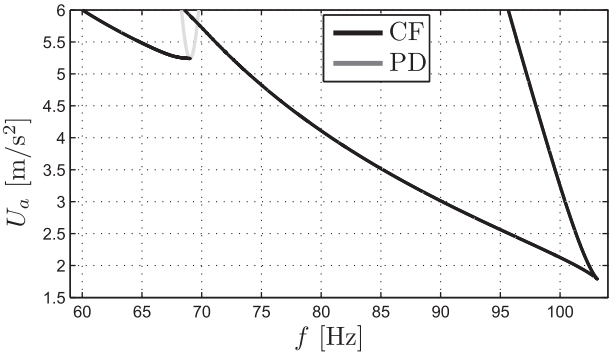

Fig. 14. Two parameter continuation diagram near the third harmonic resonance ($f_{03} = 104.1$ Hz).

9.3. Poincaré maps

Initial value problems are solved in order to examine possible a-periodic steady-state responses in the frequency interval enclosed by the PD bifurcations at $f = 9.82$ Hz and $f = 10.60$ Hz respectively for $U_a = 1.0$ m/s^2. This is also carried out for the frequency interval enclosed by the SH bifurcations at $f = 79.92$ Hz and $f = 97.47$ Hz respectively for $U_a = 6.0$ m/s^2. For both cases, starting at the stable side of the right bifurcation point, the excitation frequency is stepwise decreased with a frequency step of $\Delta f = 0.05$ Hz. The effect of transient responses is minimized by disregarding the solution for the first 15 s after each time the excitation frequency is changed. The resulting steady-state responses are used to construct Poincaré maps, by taking snapshots of the solution at $t = T, 2T, \ldots, N_p T$, where $T = 1/f$, and plotting the result in a two-dimensional subspace spanned by h_z and $\dot{h}_z$. Each Poincaré map contains $N_p = 2000$ points.

Fig. 10 shows several Poincaré maps in the frequency interval $9.81 \leqslant f \leqslant 10.63$ Hz and for an acceleration amplitude of $U_a = 1.0$ m/s^2. The harmonic solution at $f = 10.63$ Hz experiences a transition to a 1/2,1/4, and 1/8 subharmonic response if the excitation frequency is incrementally decreased. This behavior suggests an infinite cascade of PD bifurcations, also known as the Feigenbaum route to chaos (Feigenbaum, 1983), which results in a solution with chaotic behavior at $f = 10.54$ Hz. Solutions with a

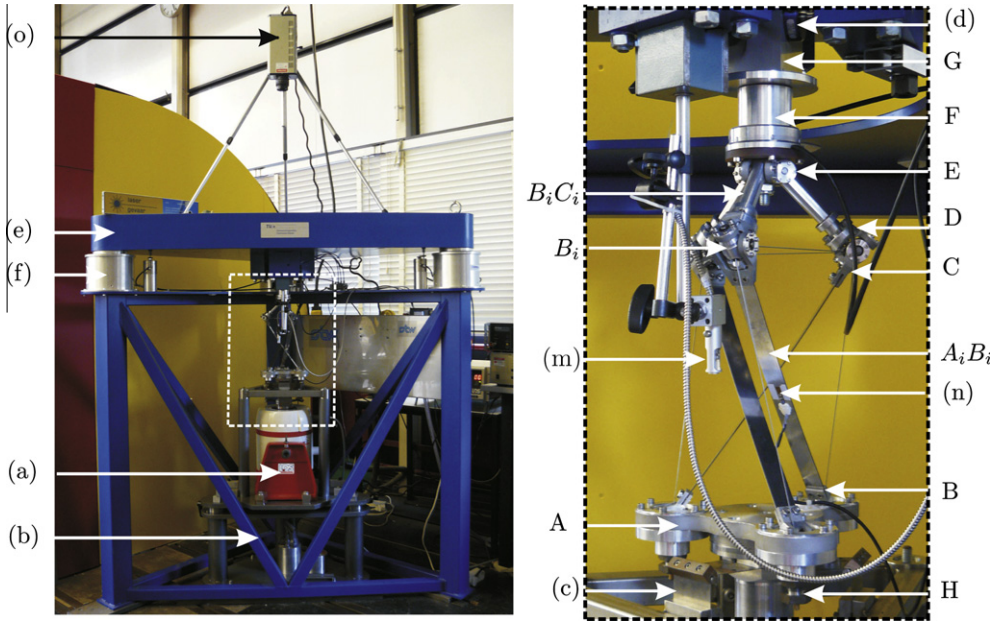

Fig. 15. The experimental set-up (upper picture) and an enlargement of the shaker, tensegrity structure, and top mass (lower picture).

chaotic nature remain visible up to the frequency close to the left PD bifurcation at $f = 9.82$ Hz. Note that in Mallon et al. (2008, 2010), where the dynamic stability of a cylindrical shell carrying a top mass is investigated, similar phenomena are encountered. Also there, the first harmonic resonance peak becomes unstable for an increasing amplitude of the harmonic base excitation and a-periodic responses are found.

For $U_a = 6.0$ m/s^2, Fig. 11 shows several Poincaré maps at frequencies within the frequency interval enclosed by the SH bifurcations at $f = 79.92$ Hz and $f = 97.47$ Hz. Harmonic responses are found just outside this frequency interval. The Poincaré maps at $f = 95.17$ Hz and $f = 80.77$ Hz show low order subharmonic responses, characterized by a discrete number of Poincaré points. Quasi-periodic solutions (closed curves) are visible in the remaining Poincaré maps.

9.4. Two-parameter continuation diagrams

The change of the loci of bifurcations of the periodic solutions can be studied by performing parameter continuation in a two parameter space, see Doedel (2007). In this way, upper bounds on the acceleration amplitude can be found so that nonlinear response phenomena due to CF and PD bifurcations (sudden jumps in response amplitudes, 1/2 subharmonic resonances, and a-periodic behavior) can be avoided.

For base excitation amplitudes $U_a \leqslant 6.0$ m/s^2, the two-parameter continuation diagram is divided in four frequency regions, i.e. in the vicinity of the three eigenfrequencies f_{0k}. The results are depicted in Figs. 12–14. In these figures, the loci of CF bifurcations are depicted with black curves and the loci of PD bifurcations with gray curves. The left plot of Fig. 12 shows that the second superharmonic resonance peak near $f \approx f_{01}/2$ starts to exhibit softening effects if $U_a \geqslant 4.22$ m/s^2. The 1/2 subharmonic resonance peak near $f \approx 2f_{01}/3$ emanates if $U_a \geqslant 4.14$ m/s^2. The two PD bifurcations near the first harmonic resonance become visible if $U_a \geqslant 0.56$ m/s^2, see the right plot of Fig. 12. Recall that in the frequency domain enclosed by these PD bifurcations, solutions with a chaotic nature are most probably present if $U_a \geqslant 1.0$ m/s^2. Fig. 13 shows that the second harmonic resonance peak contains two CF bifurcations if $4.88 \leqslant U_a \leqslant 5.38$ m/s^2, three CF bifurcations if $U_a > 5.66$ m/s^2, four CF bifurcations if $5.38 < U_a \leqslant 5.43$ m/s^2, and five CF bifurcations if $5.43 < U_a \leqslant 5.66$ m/s^2. The 1/2 subharmonic resonance peak related to f_{01} is encountered if $U_a \geqslant 5.43$ m/s^2, for which values two PD bifurcations exist. Fig. 14 shows that the third harmonic resonance peak near $f_{03} = 104.1$ Hz starts to exhibit softening effects if $U_a \geqslant 1.79$ m/s^2. The 1/2 subharmonic (parametric) resonance near $f = 2f_{02}$ starts to grow for $U_a \geqslant 5.79$ m/s^2.

10. Experimental set-up

The remainder of this paper focusses on validation of the model, derived in Sections 2–4, by comparing experimentally and numerically obtained steady-state responses. The values of a_1, a_3, H, W, L_1, L_2, l_{oc}, and l_{oh}, presented in Table 1, are adopted in the tensegrity structure design. The experimental set-up and an enlargement of the tensegrity structure are shown in Fig. 15.

An electrodynamic shaker (a) is fixed to the upper part of table (b), which is rigidly connected to the floor. The shaker contains a massive exciter housing and a moving armature. It is driven by an amplifier operating in voltage-mode. A prescribed (harmonic) amplifier input voltage

$$V_0(t) = v_d \sin(2\pi f t) \tag{47}$$

where v_d is the excitation amplitude in [V] and f is the excitation frequency in Hz, results in an amplifier output voltage $V(t)$, which serves as the input for the shaker. Voltage $V(t)$ results in a current $I(t)$ through the coil of the shaker. This current generates a vertically directed force working on the shaker armature, which results in acceleration $\ddot{u}(t)$ of the armature. Input signal generation and data-acquisition is performed using a laptop with MATLAB2008a/Simulink in combination with two *TUeDACS Microgiant* devices (Franken, 2008).

Part E of the tensegrity structure (containing nodes C_i) is fixed to connector part F, which allows rotations around the vertical axis by two integrated ball bearings placed in parallel. Pure vertical translation of triangular block G is realized by a guide mechanism with six air bearings (d) in the center of plate (e). It is stressed that plate (e) with a weight of approximately 1000 kg, is isolated from vibrations of the environment and vibrations of the shaker by using three active air bearings (f).

In the design of the tensegrity structure, the buckling direction of beams A_iB_i matches with the buckling direction of the model, all compressive and tensile members are (dominantly) loaded in the axial direction, and the members are connected to each other by multiple ball bearings in order to keep friction forces as low as possible. Base plate A is rigidly fixed to the shaker armature. Three insets, each connected with a ball bearing to base plate A, are used to enable rotation $\alpha_i(t)$ of beams A_iB_i. The combined mass of one inset and ball bearing is denoted by m_{A_i}. The lower ends of the slender beams A_iB_i ($H \ll W \ll L_1$) with rectangular cross sections are attached to (three) parts B. Parts B are coupled to the insets in base plate A by pin-joints. The upper ends of beams A_iB_i are rigidly attached to (three) parts C. Parts C are connected by pin-joints to nodes B_i. As a result, the buckling direction of the pinned–pinned beams A_iB_i is predefined in the $\vec{e}^1_{z_i}$-direction. Each node B_i has a connection structure consisting of three tendon fixation points to ensure that the virtual intersection point of the tendons is located in nodes B_i. The connection between parts C, the connection structure of nodes B_i, and parts D can be interpreted as a cardan joint with two rotational DOFs. Rotation of parts D around the axes of struts B_iC_i is enabled by integrating two ball bearings placed in parallel inside parts D.

The geometrical imperfections of the three beams A_iB_i are measured and equal to $h_0 = -1.1$ mm, $h_0 = -0.9$ mm, and $h_0 = -0.85$ mm respectively. Indeed, the geometrical shape imperfections have approximately the shape as defined in Eq. (11). The different geometrical shape imperfections result in a slightly asymmetric tensegrity structure. This asymmetry can be removed to a large extend by altering the amount of pretension in the three cross tendons. To realize this, three bolts H, see Fig. 15, are located at the bottom side of base plate A and three additional bolts are used to secure bolts H in order to avoid that the initial pretension level of the cross tendons changes during dynamical experiments.

The masses of some parts of the tensegrity structure are listed in Table 3. It is assumed that the total mass of the base plate m_b is the sum of m_A, the mass of plate A, and $3m_{A_i}$, the masses of the three ball bearings in the horizontal plane plus the corresponding insets, which support parts B, so $m_b = m_A + 3m_{A_i}$. Beams A_iB_i are manufactured from spring steel. Each tendon is flexible and contains 140 steel twisted thin wires. The remaining components are made from aluminium. The total top mass m_3 contains the mass of part E, the mass of connector part F, the mass of triangular block G, the mass of an angular velocity sensor, and a possible additional mass, so that $m_3 \geqslant 1.210$ kg. Note that approximately 0.4 kg of the top mass can both rotate around and translate in the vertical direction and that the remaining part only can translate in vertical direction. The translating part of the top mass can be increased by mounting the additional mass on top of the vertically moving triangular block G.

The following quantities are measured during the experiments: (1) the base velocity $\dot{u}(t)$ (measured with laser vibrometer (m), see Fig. 15), (2) the angular velocity $\dot{\theta}_i(t)$ (measured with a gyroscope sensor, integrated in connector part F), (3) the transversal displacement $h_{mid}(t)$ of beam A_1B_1 measured halfway the length of this beam (indirectly measured with a calibrated strain-gauge (n)), and (4) the absolute velocity of the top mass, indicated by $\dot{h}_{z+u}(t)$ (measured with laser vibrometer (o)). Note that $\dot{h}_z(t) = \dot{h}_{z+u}(t) - \dot{u}(t)$. The velocity signals are integrated over time to obtain the corresponding displacement/rotation signals. To avoid drift during time integration, the measured velocity signals are passed through a second order high-pass frequency filter with a cut-off frequency of $f_c = 1.5$ Hz. The effect of transient responses in stepped frequency-sweep experiments is minimized by neglecting the responses of the first 75 excitation periods for each excitation frequency. Finally, the position signals are used to compute the average peak-to-peak values of a steady-state solution, containing the responses of 150 excitation periods, for each excitation frequency.

Table 3
Masses of some parts the experimental tensegrity structure. The masses of parts B, C, D, and E include ball bearing masses.

Description	Value	Unit
Base plate	$m_b = 1.356$	kg
Inset + (horizontal ball bearing)	$m_{A_i} = 27 + 33 = 60$	g
Part B + beam A_iB_i+part C	$m_{A_iB_i} = 28 + 42 + 32 = 102$	g
Connection structure in node B_i	$m_{B_i} = 15$	g
Part D + strut B_iC_i	$m_{B_iC_i} = 64 + 42 = 106$	g
Cross tendon	$m_{l_c} = 8$	g
Horizontal tendon	$m_{l_h} = 2$	g
Part E	$m_E = 40$	g

10.1. Amplifier-Shaker-Tensegrity structure model

In the experiments, the acceleration $\ddot{u}(t)$ of the base is not proportional to the prescribed input voltage $V_0(t)$ because the shaker has its own dynamics. Consequently, the dynamics of the amplifier and shaker have to be taken into account, resulting in an amplifier-shaker-tensegrity structure model. For a detailed description of the modeling of the amplifier-shaker-structure system is referred to Mallon (2008, 2010) and Fey et al. (2011). The equations of motion of the shaker in combination with the structure under investigation are derived by extending the nine dependent DOFs $\mathbf{q}$ of Eq. (21), with two independent DOFs describing the dynamics of the electrodynamic shaker, namely the charge $q(t)$, i.e. the integral over time of the current $I(t) = \dot{q}(t)$, and the position $u(t)$ of the shaker armature, i.e. the base. In general form, the equations of motion of the amplifier-shaker-tensegrity structure are

$$L_c\ddot{I} + R_cI + \kappa_c\dot{u} = V(t) = P_a(V_0(t) + b_a\dot{V}_0(t)) \tag{48}$$

$$m_s\ddot{u} + c_s\dot{u} + k_su = \kappa_cI + F_{ten} \tag{49}$$

where L_c is the coil inductance, R_c is the coil resistance, κ_c is the current-to-force constant, P_a and b_a are the amplifier coefficients, m_s is the translating mass of the shaker, c_s is the mechanical damping constant of the shaker, k_s is the spring stiffness of the shaker, and F_{ten} is the vertical force exerted on the shaker mass by the tensegrity structure.

11. Parameter identification

The parameter values of the amplifier-shaker model are identified in Section 11.1 by using experiments on the bare shaker. In Section 11.2, some of the parameter values of the tensegrity structure are identified by using measurements on the total experimental set-up.

11.1. Amplifier-shaker identification

Based on static experiments on the bare shaker, it can be concluded that the shaker stiffness k_s is linear for the displacement range of interest. The remaining parameters

$$\mathbf{c}_s = [\, m_s \quad c_s \quad L_c \quad \kappa_c \quad R_c \quad P_a \quad b_a \,]^T \tag{50a}$$

are identified by minimizing functional J, representing a sum of squared differences between the real and imaginary parts of the numerical FRF $H_{\Delta\ddot{u}\Delta V_0}$ and the measured FRF $\widehat{H}_{\Delta\ddot{u}\Delta V_0}$ of the bare shaker

$$J(\mathbf{c}_s) = \mathbf{r}(\mathbf{c}_s)^T\mathbf{r}(\mathbf{c}_s) \tag{50b}$$

where $\mathbf{r}(\mathbf{c}_s)$ is the weighted residue column specified at N discrete frequency points in the frequency interval $2.5 \leqslant f \leqslant 120$ Hz

$$\mathbf{r} = \begin{bmatrix} w_1 Re(H_{\Delta\dot{u}\Delta V_0}(f_1, \mathbf{c}_s) - \widehat{H}_{\Delta\dot{u}\Delta V_0}(f_1)) \\ \vdots \\ w_N Re(H_{\Delta\dot{u}\Delta V_0}(f_N, \mathbf{c}_s) - \widehat{H}_{\Delta\dot{u}\Delta V_0}(f_N)) \\ w_1 Im(H_{\Delta\dot{u}\Delta V_0}(f_1, \mathbf{c}_s) - \widehat{H}_{\Delta\dot{u}\Delta V_0}(f_1)) \\ \vdots \\ w_N Im(H_{\Delta\dot{u}\Delta V_0}(f_N, \mathbf{c}_s) - \widehat{H}_{\Delta\dot{u}\Delta V_0}(f_N)) \end{bmatrix} \tag{50c}$$

Weighting functions $w_n = 1/|\widehat{H}_{\Delta\dot{u}\Delta V_0}(f_n)|$ for $n = 1,\ldots,N$ are introduced to equally distribute the relative error of the residue vector over the whole frequency range.

Responses of the bare shaker resulting from white noise excitation are used to estimate the experimental FRF $\widehat{H}_{\Delta\dot{u}\Delta V_0}$, where $\Delta\dot{u}$ is the velocity of the base and ΔV_0 is the white noise amplifier input voltage. The influence of disturbance noise is reduced by averaging over 225 records, where each record contains 2^{14} points. The mass of the shaker armature is increased by fixing an additional mass of 1.381 kg to it. In this way, the effect of the mass of the base plate of the tensegrity structure, $m_b = 1.356$ kg, is taken into account in the identification procedure of the amplifier-shaker model. The identified parameter values $\mathbf{c}_s^*$ are presented in Table 4.

11.2. Tensegrity structure identification

For identification purposes, FRFs $\widehat{H}_{l,k}$ of the experimental set-up are measured for $k = 1,\ldots,N_m = 11$ top masses. Here, subscript l refers to a specific input–output relation, namely $l = 1$ corresponds to $\widehat{H}_{\Delta u\Delta V_0}$, $l = 2$ corresponds to $\widehat{H}_{\Delta\theta\Delta V_0}$, $l = 3$ corresponds to $\widehat{H}_{\Delta h_{mid}\Delta V_0}$, and $l = 4$ corresponds to $\widehat{H}_{\Delta h_z\Delta V_0}$. The relation between subscript k and the top mass is depicted in Table 5. Each FRF corresponding to a certain top mass is obtained by averaging over 210 records, where each record contains 2^{16} points.

The measured FRFs are, first of all, used to determine the modal parameters of the experimental set-up based on a multi-DOF modal parameter fit in the frequency domain with four dominant modes, indicated by subscript i. The experimental eigenvalues $\hat{\lambda}_{i,k} = \hat{\mu}_{i,k} + \hat{\nu}_{i,k}j$ are used to derive the experimental dimensionless damping coefficients for the eleven top masses based on the relation $\hat{\xi}_{i,k} = -\hat{\mu}_{i,k}/\sqrt{\hat{\mu}_{i,k}^2 + \hat{\nu}_{i,k}^2}$. In the eigenmodes corresponding to eigenvalues $\lambda_{1,k}$, $\lambda_{3,k}$, and $\lambda_{4,k}$, resonances in the tensegrity structure are dominant (note that three eigenmodes indeed correspond to three independent DOFs). In the eigenmode corresponding to $\lambda_{2,k}$, resonance of the shaker armature/base plate is dominant. In addition to these eigenvalues and eigenmodes, which occur in complex conjugate pairs, one real eigenvalue and corresponding eigenmode is strongly related to the electric part of the shaker model. In the latter eigenmode, the current is dominant.

It appears that ξ_3 and ξ_4 are approximately linearly dependent on the top mass, whereas ξ_1 is approximately independent of the top mass. These observations are used by introducing two linear relations for ξ_3 and ξ_4, which depend on the top mass

$$\xi_3(m_3) = \xi_{30} + \xi_{31} m_3 \tag{51}$$

$$\xi_4(m_3) = \xi_{40} + \xi_{41} m_3 \tag{52}$$

Note that the mechanical damping parameter of the shaker, corresponding to ξ_2, already has been identified in Section 11.1.

Next, a number of unknown parameters $\mathbf{c}_t$ of the amplifier-shaker-tensegrity structure model, linearized around the static equilibrium points for the eleven top masses, is estimated using measured FRFs. To be more specific, the parameter values of the initial stress-free tendon length l_{oc}, the cross and horizontal tendon stiffness k_c and k_h, the critical axial buckling load P_c, the effective mass $m_{1e} = \rho_{1e}WHL_1$ of beams A_iB_i, the effective mass $m_{2e} = \rho_{2e}\pi R^2 L_2$ of struts B_iC_i, and the dimensionless damping parameter related to ξ_i with $i = 1,3,4$ are estimated. Note that identification of effective masses m_{1e} and m_{2e} in fact means that effective mass densities ρ_{1e} and ρ_{2e} are identified. In this way, additional masses in the experimental set-up, which are absent in the model, are taken into account. The unknown parameters are collected in

$$\mathbf{c}_t = [l_{oc} \quad k_c \quad k_h \quad P_c \quad m_{1e} \quad m_{2e} \quad \xi_1 \quad \xi_{30} \quad \xi_{31} \quad \xi_{40} \quad \xi_{41}]^T \tag{53}$$

The identification method is divided into two steps due to the complex linearized dynamics of the amplifier-shaker-tensegrity structure model. In the first step, the squared difference between the numerical and experimental eigenvalues, $\lambda_{i,k}(\mathbf{c}_t) = \mu_{i,k} + \nu_{i,k}\,j$ and $\hat{\lambda}_{i,k} = \hat{\mu}_{i,k} + \hat{\nu}_{i,k}j$ respectively, is minimized in order to determine a suitable initial guess $\mathbf{c}_t^0$ of the unknown parameter values. In the second step, the initial guess $\mathbf{c}_t^0$ is used to identify the final parameter values $\mathbf{c}_t^*$ of the tensegrity structure. This step is based on a similar optimization method as presented in SubSection 11.1. In this case, the optimization method includes all measured FRFs for all top masses, i.e. $l = 1,\ldots,4$ and $k = 1,\ldots,N_m$. The resulting identified parameter values are listed in Table 6.

12. Model validation

Numerical results based on the identified amplifier-shaker-tensegrity structure model are compared with experimentally obtained eigenvalues in Section 12.1, experimentally obtained FRFs in Section 12.2, and experimentally obtained frequency-amplitude plots based on stepped frequency sweep-up and sweep-down measurements in Section 12.3. Recall that in the experimental set-up, a small part of the top mass can both rotate and translate, whereas rotational inertia was not modelled. The justification of

Table 4
Identified parameter values $\mathbf{c}_s^*$ of the amplifier-shaker model.

Parameter	Value	Unit
m_s	1.7295	kg
k_s	4.30×10^4	N/m
c_s	162.33	kg/s
L_c	2.258×10^{-3}	H
κ_c	9.0076	N/A
R_c	0.920	Ω
P_a	−74.97	–
b_a	1.515×10^{-3}	s^{-1}

Table 5
The relation between subscript k and the top mass m_3.

k	m_3	Unit	k	m_3	Unit
1	1.442	kg	7	4.450	kg
2	1.933	kg	8	4.935	kg
3	2.421	kg	9	5.423	kg
4	2.994	kg	10	6.019	kg
5	3.482	kg	11	6.507	kg
6	3.962	kg			

Table 6
Identified parameter values $\mathbf{c}_t^*$ of the tensegrity structure.

Parameter	Value	Unit	Parameter	Value	Unit
l_{oc}	25.167	cm	ξ_1	0.0638	–
k_c	95.8	kN/m²	ξ_{30}	0.0341	–
k_h	112.9	kN/m²	ξ_{31}	−0.0035	kg^{-1}
P_c	63.8	N	ξ_{40}	0.0553	–
m_{1e}	40	g	ξ_{41}	−0.0045	kg^{-1}
m_{2e}	232	g			

this model simplification has been checked. The translational inertial force of the top mass has dominant influence on the dynamic response compared to the (small) rotational inertial moment of the lower part of the top mass. Moreover, rotational inertia of the remainder of the (moving part of the) structure dominates the neglected rotational inertia of the lower part of the top mass.

12.1. Eigenvalues

Fig. 16 shows the experimental eigenvalues $\hat{\lambda}_{i,k}(m_3)$ (black markers) obtained from the multi-DOF modal parameter fit in the frequency domain and the numerical eigenvalues $\lambda_{i,k}(\mathbf{c}_t^*, m_3)$ (gray markers) computed with linearized dynamic models of the identified amplifier-shaker-tensegrity structure. The (real) eigenvalue corresponding to the eigenmode dominated by the electric part of the shaker is not shown and the damped eigenfrequencies are expressed in Hz by $f_i = \text{Im}(\lambda_i)/2\pi = v_i/2\pi$.

The following observations hold for the experimental as well as the numerical eigenvalues. The first eigenfrequency near $f_1 \approx 7.0$ Hz, corresponding to an eigenmode dominated by rotation around the $\vec{e}_z^0$ axis, slightly decreases for increasing top masses, whereas the second eigenfrequency near $f_2 \approx 14.0$ Hz (related to the shaker resonance) is barely influenced by changes in the top mass. The third eigenfrequency f_3, corresponding to the eigenmode, in which buckling of beams A_iB_i is dominant, increases from 31.5 Hz for m_3= 1.442 kg to 47.7 Hz for m_3= 6.507 kg. Finally, the fourth eigenfrequency f_4 has a minimum at $m_3 \approx 4.0$ kg. The observations for f_1, f_2, and f_4 match with the modal analysis results of the tensegrity structure when the shaker is excluded, see Fig. 5 in Section 7.

The imaginary parts $v_{i,k}$ of the numerical and experimental eigenvalues correspond very well. The real parts $\mu_{i,k}$ of the numerical and experimental eigenvalues are in reasonable good agreement. It can be concluded that the linearized amplifier-shaker-tensegrity structure model can be used to predict the location of the eigenvalues of the system for top masses in the range of $1.442 \leqslant m_3 \leqslant 6.507$ kg.

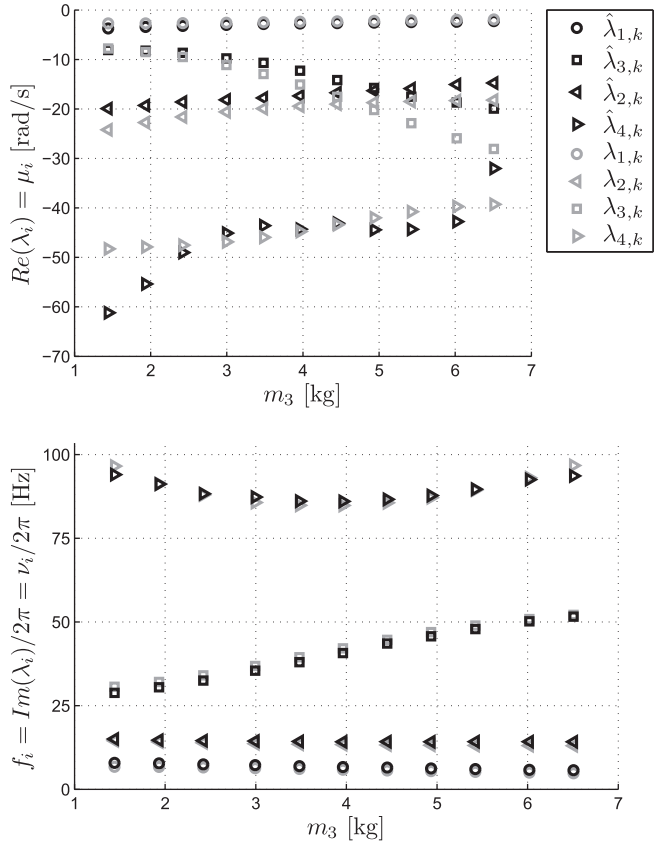

Fig. 16. Experimental eigenvalues (black markers) and the numerical eigenvalues of the tensegrity structure.

12.2. Frequency response functions

Fig. 17 shows Bode plots and coherence functions of the measured FRFs $\widehat{H}_{\Delta\theta,\Delta V_0}$ and $\widehat{H}_{\Delta h_z,\Delta V_0}$ for the frequency interval $2.5 \leqslant f \leqslant 120$ Hz and a top mass of $m_3 = 2.994$ kg. In this figure, black lines indicate measured FRF, whereas gray lines show the FRFs of the linearized identified amplifier-shaker-tensegrity structure model.

Five resonance peaks can be distinguished in the Bode plots of the measured FRFs. The heavily damped resonance peak at $f_2 \approx 13.7$ Hz corresponds to the eigenmode dominated by shaker resonance and the small resonance peak at $f_5 \approx 102.0$ Hz is due to the finite stiffness of the shaker support structure. The latter is concluded based on the measured FRFs of the bare shaker. The remaining resonance peaks near $f_1 = 7.0$ Hz, $f_3 = 35.7$ Hz, and $f_4 = 86.4$ Hz correspond to eigenmodes dominated by the tensegrity structure. It is stressed that the resonance peaks of the tensegrity structure can clearly be distinguished in all Bode plots for the eleven top masses. In general, the behavior of the coherence function is similar for all FRFs. Coherence values drop in frequencies intervals with anti-resonances. From Fig. 17, two conclusions can be drawn:

- The measured FRFs are approximated (reasonably) well in the frequency interval $2.5 \leqslant f \leqslant 80$ Hz by their numerical counterparts.
- For the frequency interval $80 \leqslant f \leqslant 120$ Hz, differences in the modulus and the phase between the experimental and numerical FRFs are observed mainly due to the small resonance in the experimental FRFs near 102 Hz, which obviously cannot be predicted by the current model.

Overall, it can be concluded that the FRFs of the amplifier-shaker-tensegrity structure model show a satisfactory correspondence with the experimental FRFs for all top masses.

12.3. Nonlinear steady-state responses

The nonlinear steady-state responses of the system, experimentally generated with stepped frequency sweeps with a harmonic input voltage according to Eq. (47), are used to determine the experimental frequency-amplitude plots. During each experiment, a frequency sweep-down is carried out (by stepwise decreasing the excitation frequency with $\Delta f = 0.1$ Hz), which is followed by a frequency sweep-up (by stepwise increasing the excitation frequency with $\Delta f = 0.1$ Hz). The nonlinear dynamic steady-state responses near the first and third harmonic resonance frequencies of the system are studied by using two top masses, i.e. $m_3 = 1.442$ kg and $m_3 = 2.994$ kg.

For the frequency range $5 \leqslant f \leqslant 18$ Hz, the experimentally obtained frequency-amplitude plots of $\tilde{\theta}$ and $\tilde{h}_z$ (black and gray dots) for $m_3 = 1.442$ kg and $v_d = 0.055$ V are presented in Fig. 18 together with the numerically obtained frequency-amplitude plots (solid and dashed black lines) based on the identified amplifier-shaker-tensegrity structure model. The first harmonic resonance peak, predicted by the model and related to the first eigenfrequency near $f = 7.0$ Hz, corresponds well to the measured first harmonic resonance peak. In Fig. 18, the softening 1/2 subharmonic resonance near 14 Hz is a combination resonance due to $2f_1 \approx f_2 \approx 14$ Hz. In the model, it occurs in a somewhat smaller frequency range than in

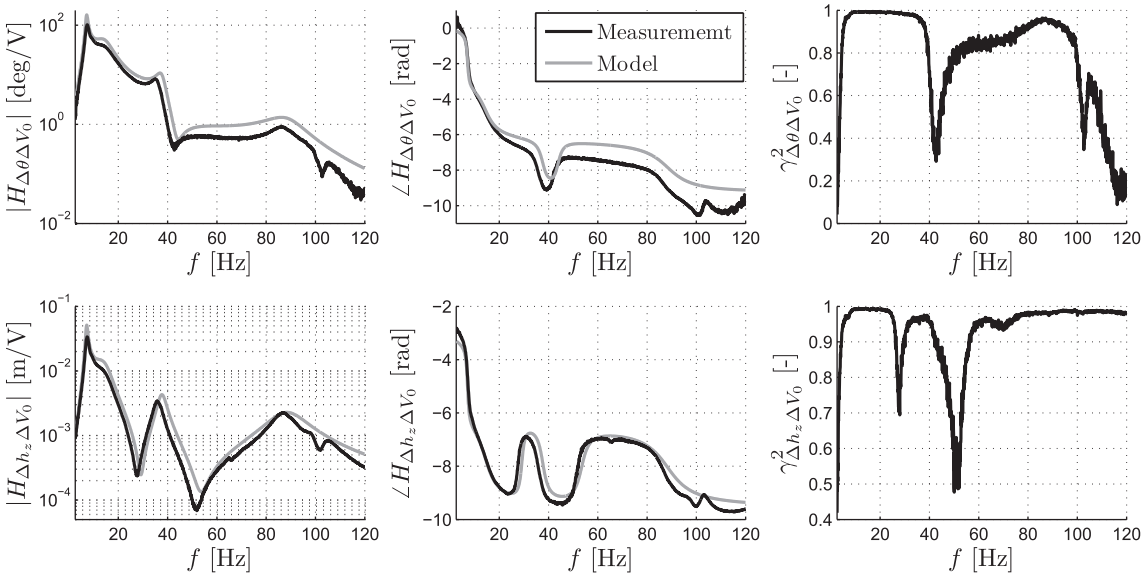

Fig. 17. Bode plot and coherence function of $H_{\Delta\theta\Delta V_0}$ (upper plots) and $H_{\Delta h_z\Delta V_0}$ (lower plots).

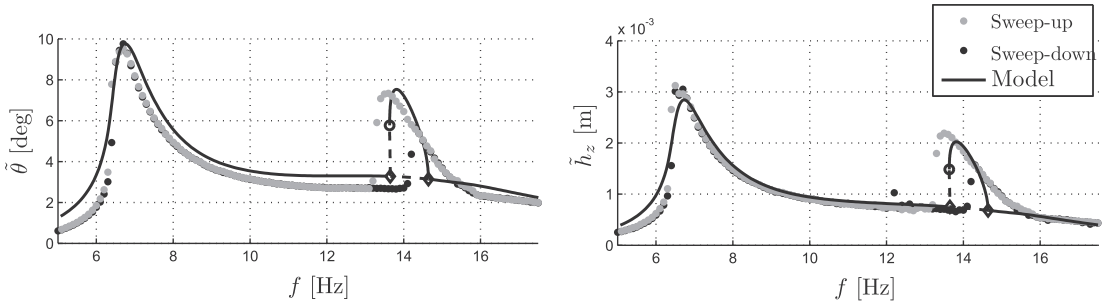

Fig. 18. Experimental and numerical frequency-amplitude plots for $m_3 = 1.442$ kg and $v_d = 0.055$ V.

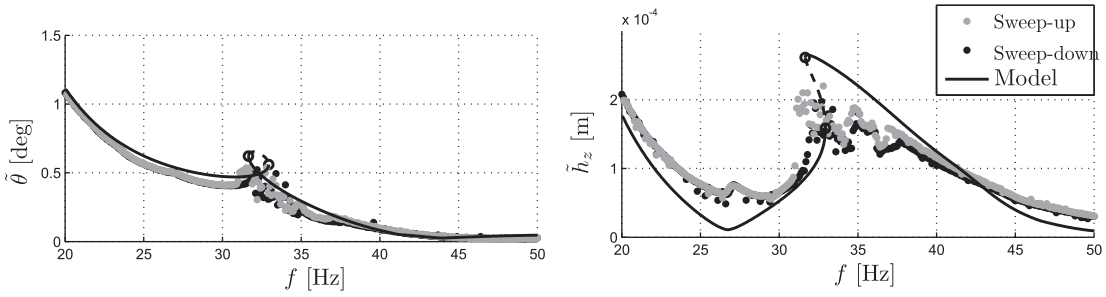

Fig. 19. Experimental and numerical frequency-amplitude plots for $m_3 = 2.994$ kg and $v_d = 0.0325$ V.

the experiment. In the experiment, the occurrence of frequency hysteresis is much clearer than in the simulation. Indeed, in the frequency sweep-up, a sudden increase in the amplitude is visible at 14.2 Hz, whereas a sudden decrease in amplitude occurs at 13.5 Hz. In the simulations, the two CF bifurcations, which are responsible for the sudden jumps, are much closer to each other. Note that very probably the 1/2 subharmonic resonance near $f = 2f_{01} = 14$ Hz is absent in Fig. 8 due to the absence of shaker dynamics there. Summarizing, in Fig. 18, despite some quantitative differences, the global nonlinear steady-state dynamics in the experiment are qualitatively comparable to the numerical responses.

Fig. 19 shows the experimentally and numerically obtained frequency-amplitude plots of $\tilde{\theta}$ and $\tilde{h}_z$ for a top mass of $m_3 = 2.994$ kg and a voltage amplitude of $v_d = 0.0325$ V. Near $f = 33$ Hz, a harmonic resonance peak is found, which is related to the third eigenfrequency at $f_{03} = 35.7$ Hz (recall that the corresponding eigenmode is dominated by buckling of beams A_iB_i). The experimental peak-to-peak values of $\tilde{h}_z$ are overestimated by the model near the resonance peak near 33 Hz and underestimated near the anti-resonance between near 27 Hz. The main reason for this is asymmetrical buckling behavior of beams A_iB_i in the experiment due to the different geometrical shape imperfections. Globally, for $\tilde{h}_z$, the experimental solution branch near the resonance peak related to the third eigenfrequency is in good agreement with the numerical solution branch. For $\tilde{\theta}$, the numerical and experimental obtained solution branches are in good agreement.

13. Conclusions

In this paper, the numerical and experimental linear and nonlinear steady-state dynamics of a base excited 3D tensegrity structure carrying a top mass (and a top mass supporting structure) are examined. The equations of motion are derived by using Lagrange's equation of motion with constraints. In this model, the compressive members (beams $A_i B_i$) of the tensegrity module are allowed to buckle and the tendons are modeled by piecewise linear springs, which can only take tensile forces. Top mass, pretension in the tendons, and geometrical and material properties of the tensegrity structure are chosen in such a way that the system is close to the static stability boundary. The effect of additional harmonic base excitation is investigated in order to study the dynamic stability of the structure.

Static responses show that static buckling of beams A_iB_i becomes more dominant for relatively large vertical compressive loads, whereas slackening of the horizontal tendons is encountered for a certain vertical tensile load. For larger loads, the static responses are characterized by geometric nonlinearities (large changes in the geometrical equilibrium configuration occur), especially with respect to the rotation around the vertical axis.

The undamped eigenfrequencies and corresponding eigenmodes are studied by linearizing the equations of motion around stable static equilibrium points for a range of top masses and by solving the corresponding eigenvalue problems for the undamped system. In addition, for a specific top mass, a linearized model is used to examine the linear dynamic responses of the system by evaluating three FRFs of the system.

Nonlinear steady-state responses of the tensegrity structure are investigated by prescribing periodic base excitation with a constant acceleration amplitude high enough to introduce nonlinear dynamic phenomena. Frequency-amplitude plots are obtained by solving two-point boundary value problems in combination with a continuation method for periodic solutions. Multiple types of nonlinear dynamic resonances are encountered such as harmonic resonance peaks (mostly characterized by softening effects), superharmonic resonance peaks, and subharmonic/parametric resonance peaks. In addition to these periodic responses, Poincaré maps suggest that quasi-periodic and chaotic solutions are also encountered near some resonance peaks. Finally, two parameter continuation diagrams of the loci of cyclic fold and period doubling bifurcations of periodic responses are presented to assess upper bounds for the harmonic excitation amplitude in order to prevent dynamic instability of the tensegrity structure.

A tensegrity structure has been designed and manufactured and an experimental set-up has been realized in order to validate the dynamic model of the tensegrity structure. The design of the tensegrity structure incorporates a predefined (static and dynamic) buckling direction of the compressive members of the tensegrity module and it ensures that the members are (dominantly) loaded in the axial direction.

To be able to compare the experimentally obtained responses to their numerical counterparts, an amplifier-shaker-tensegrity structure model is derived because the dynamics of the amplifier and shaker, used to excite the base of the tensegrity structure in the experimental set-up, interact with the dynamics of the tensegrity structure with top mass.

Numerical FRFs, computed with a linearized dynamical model of the amplifier-shaker-tensegrity structure, are in good correspondence with experimentally obtained FRFs. In addition, linearized dynamic models are used to compute the numerical eigenvalues of the system for several top masses. These eigenvalues are in good agreement with the experimental eigenvalues, which are determined by a multi-DOF modal parameter fit in the frequency domain using measured FRFs. Finally, frequency-amplitude plots based on the nonlinear dynamic amplifier-shaker-tensegrity structure model are compared with experimental frequency-amplitude plots obtained by stepped frequency sweep experiments. Globally, the measured nonlinear dynamic steady-state responses can be predicted by the model.

It can be concluded that for a tensegrity structure near the static stability boundary, linear and nonlinear dynamic steady-state responses, caused by additional periodic loads, can be predicted by the model developed in this study. Therefore, this model structure may be used as a starting point to efficiently examine the static and dynamic stability of other tensegrity structures.

Acknowledgements

Bram de Jager is gratefully acknowledged for fruitful discussions and Pieter van Hoof and Peter Hamels for the manufacturing of the tensegrity structure.

References

Adriaenssens, S., Barnes, M., 2001. Tensegrity spline beam and grid shell structures. Eng. Struct. 23, 29–36.
Aldrich, J., 2004. Control synthesis for a class of light and agile robotic tensegrity structures. Ph.D. thesis, University of California.
Doedel, J., 2007. Numerical Continuation Methods for Dynamical Systems. Department of Computer Science, Concordia University, Montreal.
Doedel, E., Paffenroth, R., Champneys, A., Fairgrieve, T., Kuznetsov, Y., Oldeman, B., Sandstede, B., Wang, X., 1998. AUTO97: Continuation and bifurcation software for ordinary differential equations (with HOMCONT). Technical report, Concordia University.
Duffy, J., Rooney, J., Knight, B., Crane, C., 2000. Review of a family of self-deploying tensegrity structures with elastic ties. Shock Vib. 32, 100–106.
Feigenbaum, M., 1983. Universal behavior in nonlinear systems. Physica 7D, 16–39.
Fey, R., Mallon, N., Kraaij, C., Nijmeijer, H., 2011. Nonlinear resonances in an axially excited beam carrying a top mass: simulations and experiments. Nonlinear Dyn. 66 (3), 285–302.
Franken, J., 2008. TUeDACS MicroGiant. Eindhoven University of Technology.
Fuller, R., 1962. Tensile integrity structures. United States Patent 3063521.
Furuya, H., 1992. Concepts of deployable structures in space applications. Int. J. Space Struct. 7, 143–152.
Kanchanasaratool, H., Williamson, D., 2002. Modeling and control of class nsp tensegrity structures. Int. J. Control 75, 123–139.
Koiter, W., 1945. Over de stabiliteit van het elastisch evenwicht. Ph.D. thesis, Delft University of Technology.
Lazopoulos, K., 2005. Stability of an elastic tensegrity structure. Acta Mech. 179, 1–10.
Mallon, N., 2008. Dynamic stability of thin-walled structures: a semi-analytical and experimental approach. Ph.D. thesis, Eindhoven University of Technology.
Mallon, N., Fey, R., Nijmeijer, H., 2008. Dynamic stability of a thin cilindrical shell with top mass subjected to harmonic base-acceleration. Int. J. Solids Struct. 45 (6), 1587–1613.
Mallon, N., Fey, R., Nijmeijer, H., 2010. Dynamic stability of a base-excited thin orthotropic cylindrical shell with top mass: similations and experiments. J. Sound Vib. 329 (15), 3149–3170.
Masic, M., Skelton, R., 2004. Open-loop controll of class-2 tensegrity towers. Proc. SPIE 5383, 298–308.
Motro, R., 1992. Tensegrity systems: the state of the art. Int. J. Space Struct. 7 (2), 75–83.
Murakami, H., 2001a. Static and dynamic analyses of tensegrity structures. Part I. Nonlinear equations of motion. Int. J. Solids Struct. 38, 3599–3613.
Murakami, H., 2001b. Static and dynamic analyses of tensegrity structures. Part II. Quasi-static analysis. Int. J. Solids Struct. 38, 3615–3629.
Oppenheim, I., Williams, W., 2001. Vibration of an elastic tensegrity structure. Eur. J. Mech. A 20, 1023–1031.
Quirant, J., Kazi-Aoual, M., Motro, R., 2003. Designing tensegrity systems: the case of a double layer grid. Eng. Struct. 25, 1121–1130.
Skelton, R., 2006. Dynamics of Tensegrity Systems: Compact Forms. In: Proceedings of the 45th IEEE Conference on Decision and Control.
Skelton, R., de Oliveira, M., 2009. Tensegrity Systems. Springer, Dordrecht.
Snelson, K., 1973. Tensegrity Masts. Shelter Publications.
Sultan, C., Corless, M., 2000. Tensegrity flight simulator. J. Guid. Control Dyn. 23, 1055–1064.
Sultan, C., Skelton, R., 2004. A force and torque tensegrity sensor. Sensors Actuators A 112, 220–231.
Sultan, C., Corless, M., Skelton, R., 1999. Peak to peak control of an adaptive tensegrity space telescope. In: Proceedings of SPIE the International Society for Optical Engineering 3667, pp. 190–201.
Thomsen, J., 2003. Vibrations and Stability; Advanced Theory, Analysis, and Tools, 2nd ed. Springer, Berlin.
Tongue, B., 1996. Principles of Vibration. Oxford University Press Inc., New York.